University of Montenegro
Faculty of Science, Department of Physics

Maja Čolović

Study of the Forward Silicon Tracker Performance in the H1 Experiment at HERA

Diploma thesis

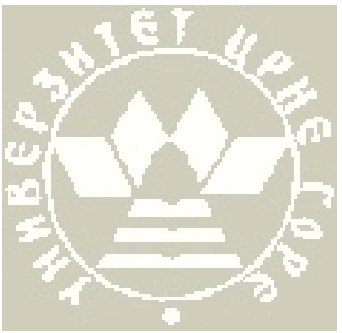

Podgorica, Serbia and Montenegro, July 2003

To my familiy

Contents

Chapter 1

Motivation

Lepton-hadron scattering experiments are used in high energy physics to investigate the structure of matter. In particular, the scattering of electrons from protons is crucial to understand the structure and binding of hadrons [fig.1.1].

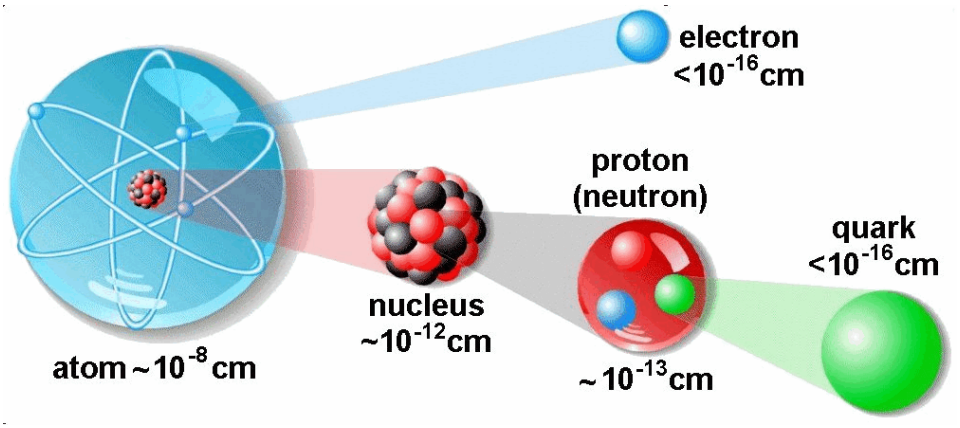

Figure 1.1: The structure of matter from the atom to the quarks

Within the Standard Model of elementary particle physics the proton consists of three point-like quarks with fractional electric charge. They interact with one another via the strong force which is described by the theory of Quantum Chromodynamics (QCD).

The most recently built facility for the study of electron-proton collisions [fig.1.2] is the Hadron Electron Ring Accelerator HERA located at the DESY laboratory in Hamburg, Germany. The measurements of the ep collision products at HERA provide a very interesting and precise insight into the partonic composition of the proton and at the same time allow the strongly coupled QCD theory to be tested.

The H1 experiment was designed to measure the scattering of electrons on protons at one of the interaction zones of HERA. During the HERA shutdown in 2000,

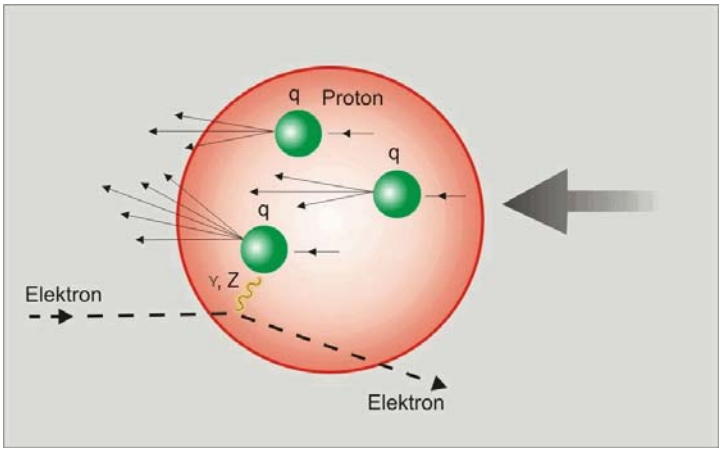

Figure 1.2: Schematic view of an electron proton collision

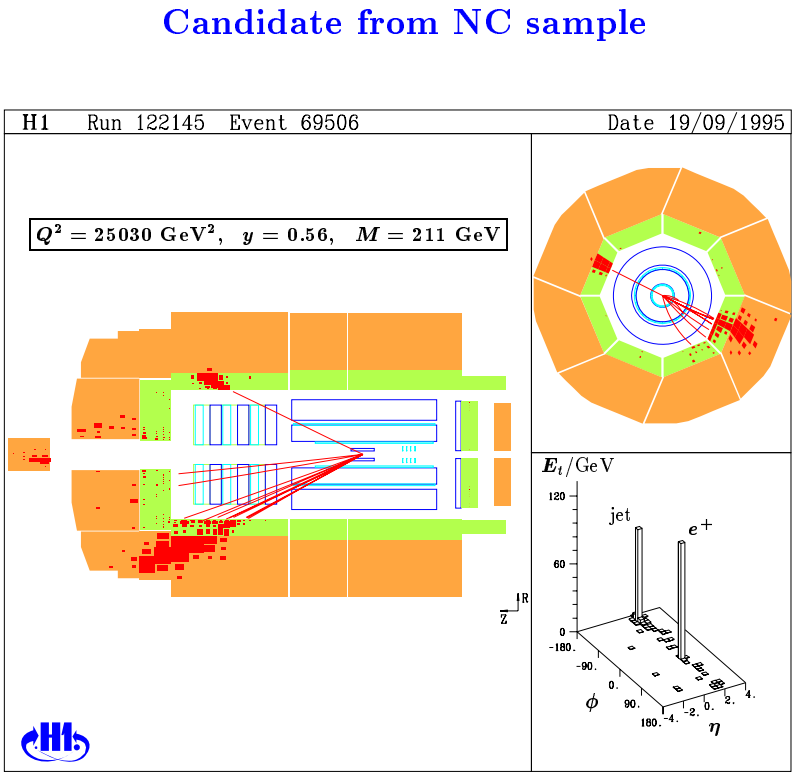

Figure 1.3: DIS event at high Q^2 = 25000 (GeV^2/c^2) where both the scattered electron and the proton fragments go in the forward direction where the FST is installed.

H1 performed a major detector upgrade and completed the existing Central and

Backward Silicon Trackers CST and BST by a Forward Silicon Tracker FST.

The **purposes of the FST** are:

1. to improve tracking in the forward direction, which means both a better measurement of the hadronic jet and of the scattered electron as shown in fig.1.3,

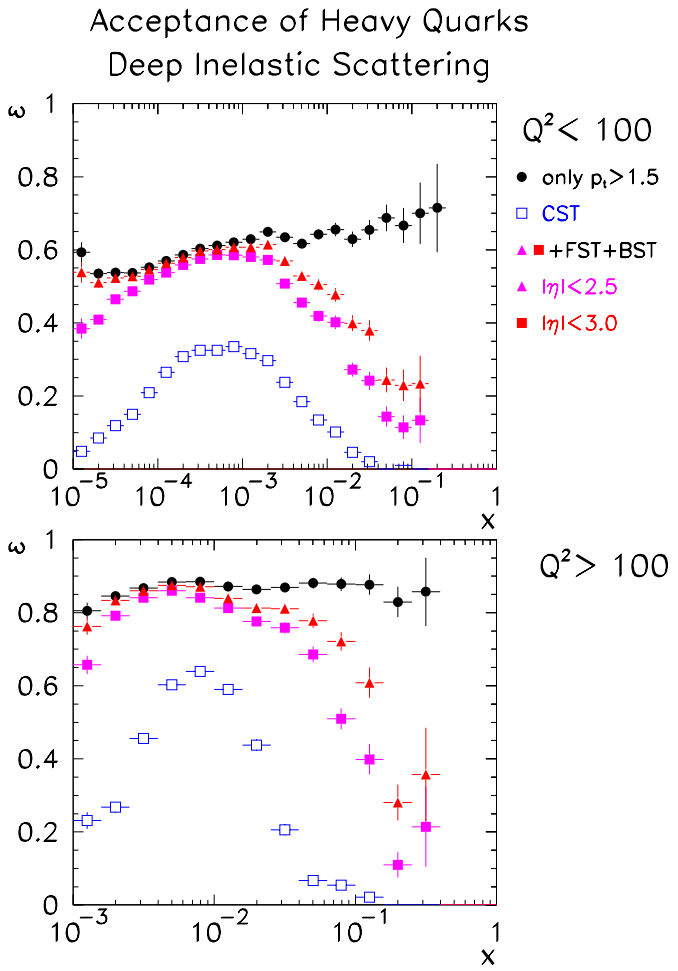

Figure 1.4: The dependence of the acceptance for charm events $D^* \rightarrow D^0\pi \rightarrow K\pi\pi$ adding BST and FST with different assumptions on the D^* acceptance

2. to improve the vertex reconstruction efficiency for the tracks that are mostly going into the forward direction,

3. to identify scattered electrons in the region of very large Q^2 as illustrated in fig.1.3. The identification of the scattered electron will profit from the reconstruction of the lepton track in the FST only. Using the Forward Tracker together with the FST the inclusive cross section measurement is expected to be precise up to the largest Q^2,

4. to extend the measurement pf charm production in the forward direction. This allows to measure the gluon density through the boson-gluon fusion process in the proton and to better understand the physics underlying fragmentation.

Inclusion of the FST into the charm particle reconstruction also allows to reconstruct charm decays using the $D^* - D$ mass difference method with a resolution of about 1 MeV [fig.4]. The Forward Silicon Tracker FST extends the acceptance for charm physics by approximately one order of magnitude into the forward direction.

In 2002 and 2003 the FST received first data from HERA. The detector readout and the hit and track reconstruction were shown to work properly [1]. Due to the HERA background conditions the useful luminosity in H1 was only of the order of an inverse picobarn so that no serious physics analysis could be performed.

For the Backward Silicon Tracker BST the precision of the momentum and angle measurement of the scattered electron can be determined by comperason with the backward calorimeter and tracking chamber. For the FST however, this is not possible due to the presence of dense forward tracks.

This give the motivation of this work: the aim was **to find simple physics objects that allow a first test of the performance and precision of the FST**. Such simple, well known processes are photon conversions and decays of neutral strange particles.

To be specific, it is the objective of this Diploma thesis **to use photon and K^0 decays to demonstrate the performance of the H1 Forward Silicon Tracker**. On top of that, the detection of ${K_S}^0$ decays opens up new charm decay channels through $D \rightarrow K^0_S \pi\pi$.

Chapter 2 describes the HERA accelerator and the H1 detector. Also, their kinematic regions are presented.
Chapter 3 gives details about the H1 tracking system. All central tracking detectors and silicon detectors are shortly described.
Chapter 4 introduces silicon as a detector material and explains mechanics, electronics and track reconstruction in the FST.
Chapter 5 presents the description of the Monte Carlo code used in this analysis. Also the track parametrisation is described and the illustration of the reconstruction steps for the K^0 meson and photon identification is given.
Chapter 6 presents the analysis that was done by Monte Carlo simulation: acceptance and efficiency of the FST for photon and neutral kaons, resolution of the vertex position, distributions of the momentum, transverse momentum as well as polar and azimuthal angles.
Chapter 7 describes the performance of the FST and of the V^0 finder code for the experimental data .
Conclusions are given in the **Summary**.

Chapter 2

The Accelerator HERA and the H1 Experiment at DESY

2.1 The ep Collider HERA

Figure 2.1: The HERA ring at DESY in Hamburg

The HERA (Hadron Electron Ring Anlage) collider shown in fig.2.1 is situated in the western suburbs of Hamburg in a nearly circular tunnel 6.3 km long. A schematic overview of HERA and its pre-accelerators is given in fig.2.2. HERA is the first and so far unique electron proton storage ring. It is the “par excellence” laboratory to study Quantum Chromo-Dynamics as the present theory of the strong interaction.

The HERA consists of two rings in which electrons at an energy of 27.5 GeV

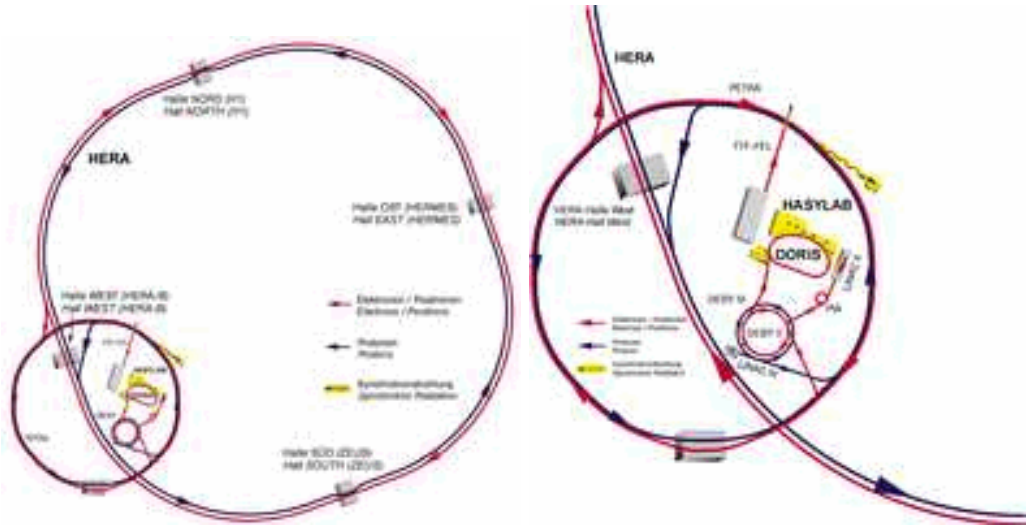

Figure 2.2: A schematic overview of DESY accelerators and storage rings: HERA (left), PETRA (right).

and protons at an energy of 920 GeV are circulated clock-wise and anti clock-wise, respectively. Its center of mass energy is $\sqrt{s}$ = 320 GeV.

The electrons with a typical current of abound 30 mA and the protons with a current of around 80 mA are stored in 180 bunches which are collided. Discrete bunches of particles are separated by 96 ns gaps. The design maximum luminosity is $1.4 \cdot 10^{30}\ cm^{-2}\ s^{-1}$.

Some bunches are left empty so that a proton or electron bunch can arrive in the detector without interaction partner. These so called pilot bunches, are used to determine background coming from a beam interaction with residual gas in the beam-pipe (beam-gas) and from collisions where beam particles interact with the beam pipe (beam-wall).

The maximum reachable energy of the stored beams is given by two different limitations. The electron energy is limited by the available accelerating power which has to compensate the strong increase of synchrotron radiation losses while the proton energy is limited by the strength of the magnetic field which is required to keep the must heavier protons on their orbit.

Positrons and protons are brought into collision in the interaction regions of the H1 and ZEUS experiments.

The H1 experiment is situated in the North Hall and the ZEUS experiment in the South Hall. Each detector consist of cylindrical central tracking chambers, surrounded by calorimeters and a tail catcher designed for muon detection. Both central tracking chambers are drift chambers. The H1 calorimeters consist of lead and steal converters in liquid argon which are located inside the superconducting solenoidal magnet which provides a magnetic field of 1.2 T.

In ZEUS, the calorimeter is a uranium-scintillator sandwich. It lies outside the solenoid within which there is a field of 1.4 T. H1 has a silicon vertex detector.

ZEUS commissioned its silicon system in 2002 [3].

There are also two fixed target experiments HERMES and HERA-B. HERMES studies the scattering of the (polarized) electron beam with a polarized hydrogen, deuterium or helium gas target. It is situated in the East Hall. HERA-B is in the fourth hall where protons collide on several possible targets. It was originally dedicated to CP violation measurements in the decay of neutral B particles. From 2002 onwards HERA-B has been devoted to measurements of the atomic number dependence of charmonium production and of the B production cross section at 920 GeV.

2.1.1 The HERA Kinematic Range

According to the Electroweak Theory charged leptons interact with the proton via an exchanged electroweak boson. In case of a neutral current interaction electrons and protons exchange a γ or Z^0 boson [fig 1.3] wheras in charged current scattering a $W^{\pm}$ boson is exchanged.

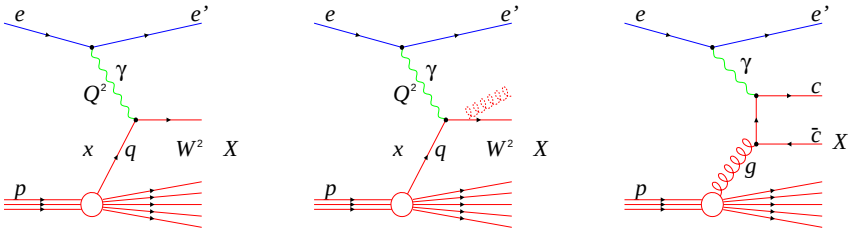

Figure 2.3: Generic Feynman diagrams for deep inelastic electron proton scattering via photon exchange. The first diagram corresponds to the simple parton model. The second diagram shows gluon radiation as a first order QCD correction. The last diagram shows heavy quark production through boson-gluon fusion.

The virtuality of the exchanged boson can be represented via the negative four momentum transfer Q^2 defined as:

$$Q^2 = -\,q^2 = -\,(e - e')^2 \tag{2.1}$$

where e and e' are the four-momenta of the incoming and outgoing lepton, respectively.

For large $Q^2 > {m_p}^2$ the proton is probed with high spatial resolution and the boson rather interacts with a constituent of the proton then with the whole.

According to Bjorken [4] this can be described with two dimensionless scaling variables x and y given by:

$$y = p \cdot q / p \cdot e \tag{2.2}$$

$$x = Q^2 / 2 \cdot p \cdot q \tag{2.3}$$

where the p is the four-momentum of the incoming proton.

In the infinite momentum frame of the proton, x is the fraction of the proton momentum carried by the struck parton. This interpretation can be extended to any other reference frame in which the proton has large momentum if the partons are assumed to be massless and have no momentum transverse to the proton direction. The inelasticity y expresses the relative loss of lepton energy in the proton rest system.

The squared invariant mass of the hadronic final state W^2, which is equivalent to the squared mass of the photon-proton system, is given by:

$$W^2 = (p + q)^2 \tag{2.4}$$

and the invariant center of mass energy squared:

$$s = (e + p)^2. \tag{2.5}$$

The kinematics of the inclusive scattering process, at fixed s, can be completely described in terms of any two independent variables. Neglecting the proton mass they are related by:

$$Q^2 = s \cdot x \cdot y \tag{2.6}$$

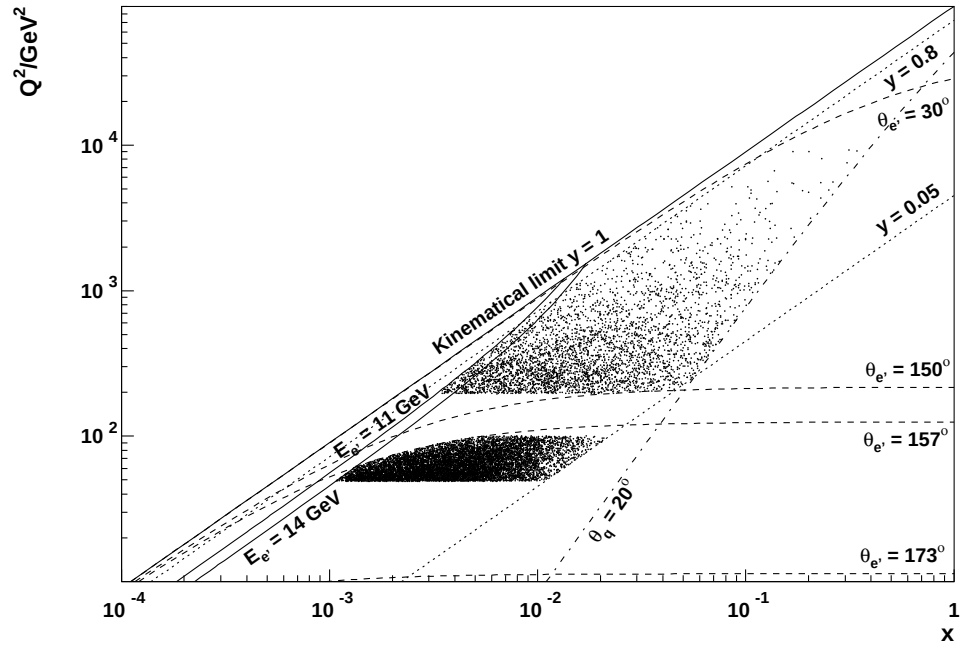

Figure 2.4: The neutral current deep inelastic scattering cross section of 27. 5 GeV electrons 960 GeV protons at the HERA accelerator as a function of x and Q^2. Shown are the iso-lines for constant energy $E_{e'}$ and constant angle $\theta_{e'}$ of the scattered electron.

The cross section for ep scattering is dominated by low Q^2 photon exchange. The amplitude for the exchange of a Z^0 and $W^{\pm}$ is compatible with photon exchange

only at Q^2 of the order $Q^2 \approx M^2(Z^0) \approx 10^4\ GeV^2$. Relevant for the FST are mainly events for high x and high Q^2 [fig.1.4].

There are three different kinematic domains defined by the virtuality of the boson exchanged between the electron and the proton:

- The photoproduction domain for $Q^2 \approx 0\ GeV^2$ corresponds to an almost real exchanged photon. Because of the small virtuality these photons fluctuate into hadronic states.
- Region of $1\ GeV^2 < Q^2 < 5000\ GeV^2$ is characterized by the exchange of a deeply virtual photon. Smaller values of x are accessed which allows extensive tests of QCD in a region where sea quark pairs are in equilibrium with gluons.
- At $Q^2 > 5000\ GeV^2$ all electroweak processes became important, including Z^0 exchange and $\gamma - Z$ interference. Due to the kinematic limits of HERA and since $Q^2 = x \cdot y \cdot s$ we have $x > 0.1$ which is the valence quarks region.

2.2 The H1 Detector

The H1 experiment is a general purpose detector composed of several subdetectors optimized for the measurement of various physical quantities. A general description can be found in [5]. In the design of the H1 detector prime attention has been given to the clean identification of electrons and to their energy measurement. To facilitate this H1 opted for a large coil, which encloses the electromagnetic and hadronic calorimeters.

Although H1 is composed like all modern collider experiments, it has an enhanced instrumentation in the proton direction which is defined as forward direction in the H1. This is a consequence of the fact that the center of mass of the collision is not at rest in the laboratory frame but progressing in the proton direction due too the highly asymmetric beam energies .

The origin of the H1 coordinate system is at the nominal interaction point inside H1 and the x-axis is pointing towards the center of the accelerator ring as shown in fig.2.5.

The experiment must also be able to distinguish ep interactions from the large backgrounds. Besides beam gas and beam wall backgrounds there is background originating from cosmic rays.

The main H1 subdetectors with increasing distances from the interaction region are shown in fig.2.6:

- Interaction region surrounded by a carbon fiber beam pipe coated with aluminum. A vacuum of the order of some picobarn minimizes strong interaction between the beam and rest gas molecules.
- The Central Tracking System consists of the Central Silicon Tracker (CST), the Central Jet Chamber (CJC), the Central Outer Z-chamber (COZ) and the Central Inner and Outer Proportional chambers (CIP and COP).

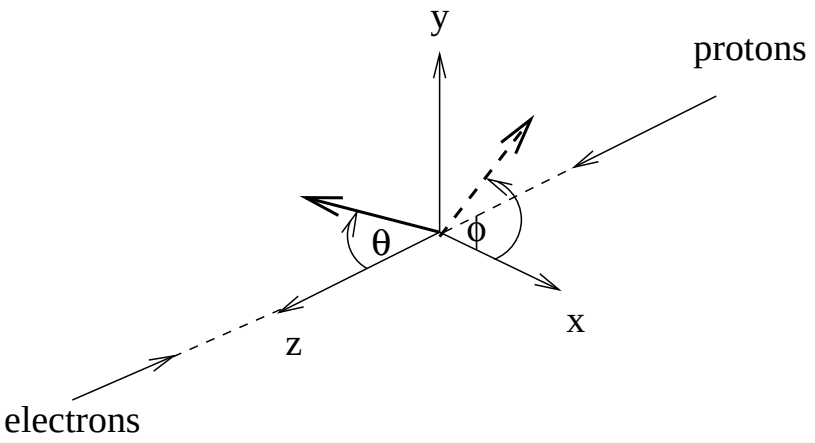

Figure 2.5: The H1 coordinate system: The positve z axis points to the proton direction. The polar angle θ of the cylindrical coordinate system is defined with respect to the z axis. The azimuthal angle ϕ is orthogonal to the z direction.

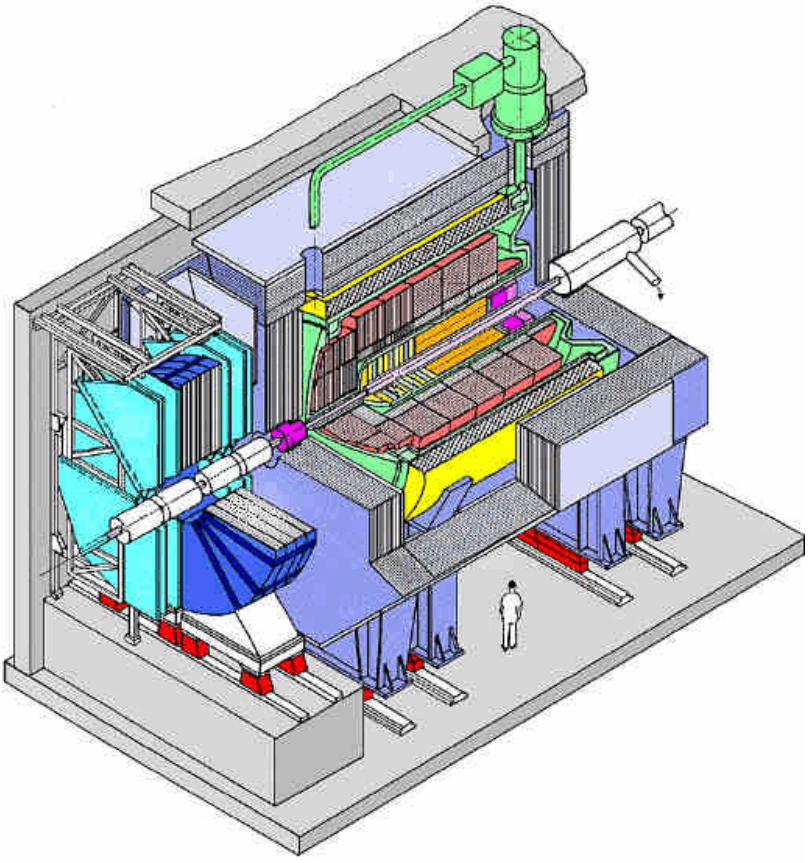

Figure 2.6: Overview of the H1 detector

- The Forward Tracker FTD
- The Electromagnetic and Hadronic part of the Liquid Argon calorimeter
- The superconducting coil which generates a homogeneous magnetic field of 1.15 T
- The lead-scintillator spaghetti calorimeter.

Every event in the H1 experiment is validated by a system of triggers. In just one out of a million bunch crossings an interesting ep interaction occurs. The task of the H1 trigger system is to discriminate these events from the large background [6]. The pipelined multi-level trigger system is designed to minimize the dead time emerging from the read out of the detector signals for which the data acquisition has to be stopped.

The H1 data acquisition system finally collects about 100 KB of raw data per event and write about 10 events per second on tape giving a data recording rate of more then 1 MB/s.

Chapter 3

The H1 Tracking System

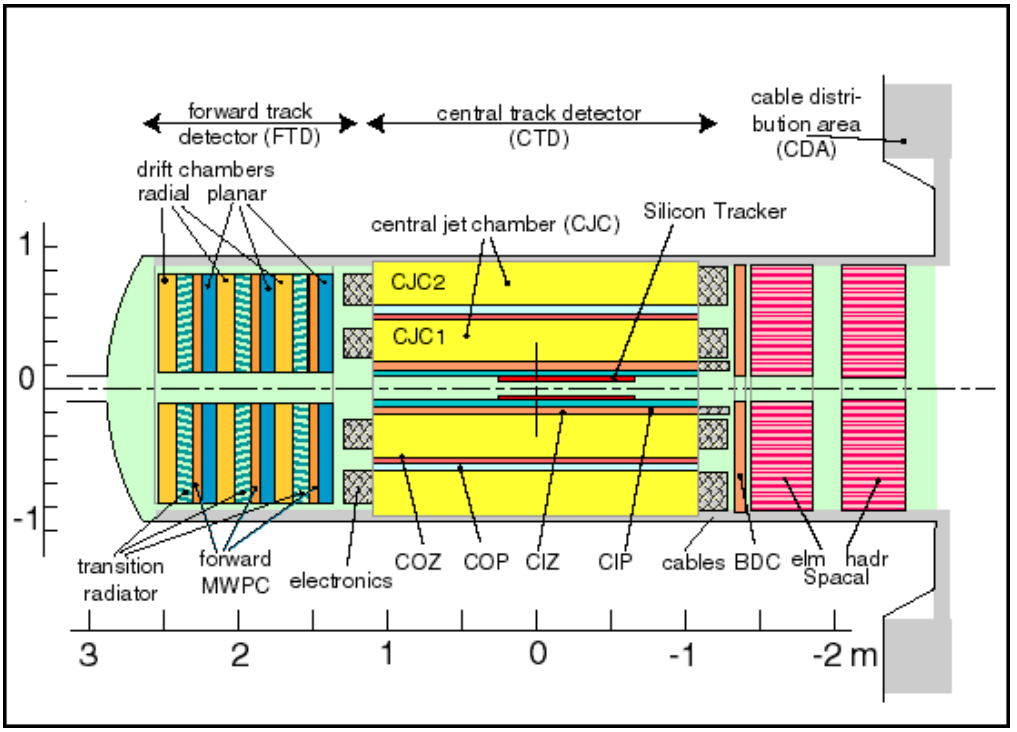

Figure 3.1: Overview of the H1 Central Tracking system

The tracking system of H1 provides simultaneous track triggering, reconstruction and particle identification for the event topology particular to HERA e-p collisions. It has been designed to reconstruct jets with high particle densities and to measure the momentum and angles of charged particles to a precision of $\sigma_{p_T}/{p_T}^2 < 0.003$ GeV^{-1} and $\sigma_\theta \approx 1 mrad$.

Because of the asymmetry between the electron and proton beam energies many charged particles are produced at small polar angles to the incident proton direction. To maintain good efficiency for triggering and reconstruction over the whole solid angle, the tracking system is divided in to a forward, central and a backward region.

The tracking system at H1 has three main types of tracking detectors: multi-wire proportional chambers (MWPCs), drift chambers and silicon trackers. Drift chambers provide accurate positional information at resolutions of the order of 100 μm. Due to the relatively large drift times (up to around 1μs) their timing information is not prompt enough for the needs of fast triggering which should ideally be faster than the time for one bunch crossing. This weakness is compensated by MWPCs which provide prompt timing information but poorer spatial resolution.

3.1 Central and Forward Track Detectors

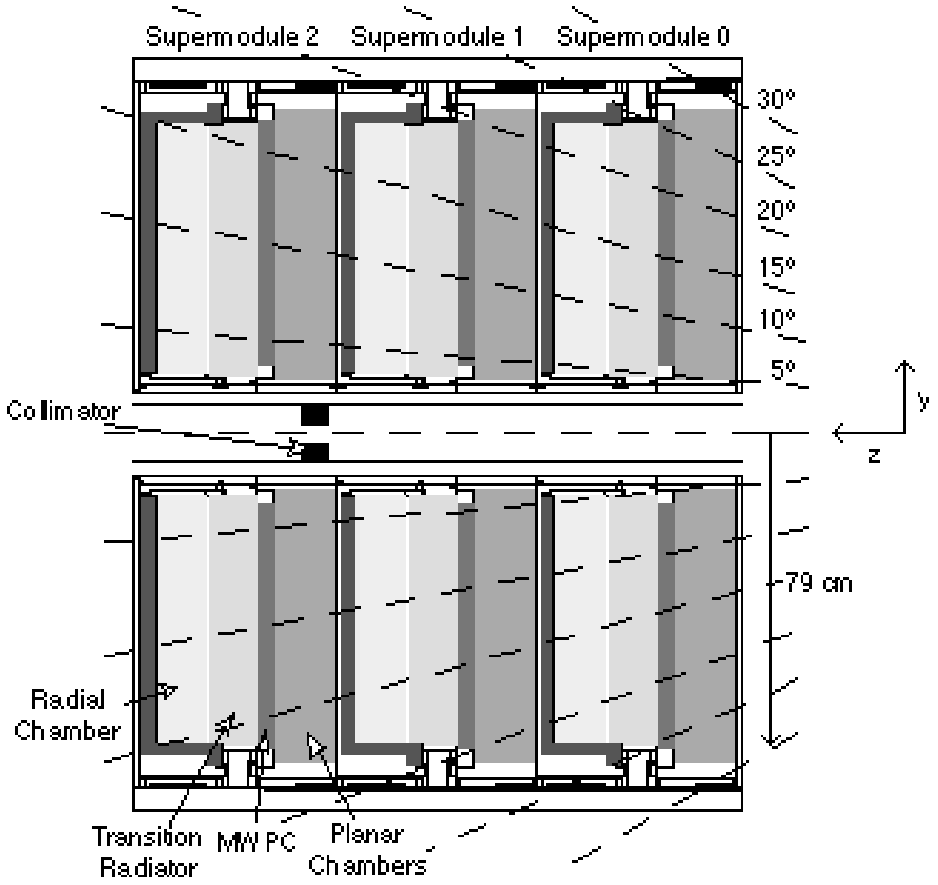

Figure 3.2: The H1 Forward Tracker

Fig.3.1 gives an overview of the Central Track Detectors. The main component are two large drift chambers , CJC1 and CJC2 [7] . Their sense wires run parallel to the beam to give best measurement along the drift direction in the transverse to beam and magnetic field. These detectors are formed from planar cells inclined at 30^0 with respect to the radial direction .

The CJC1 has 30 cells with 24 sense wires each, while CJC2 has 60 cells each containing 32 sense wires. All sense wires are read out at both ends and yield a

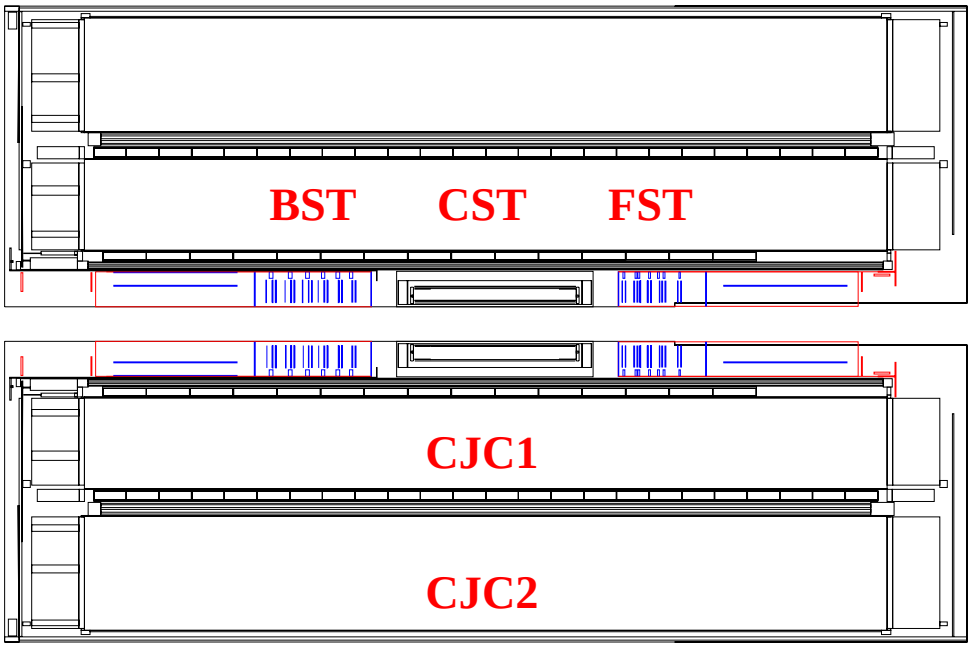

Figure 3.3: GEANT simulation structure of the H1 Central Tracker with the drift chambers CJC1, CJC2 and the three Silicon trackers FST, CST and BST.

z measurement via charge division. Drift times and charge division measurements achieve space point solutions in the $x-y$ and z planes of $170\ \mu m$ and 2.5 cm respectively.

The track recognition in the CJC is based mainly on the more precise $r-\phi$ information.The track parameters are constrained by imposing a common interaction vertex requirement. The tracks which fail are assigned either to a secondary vertex or left as non vertex fitted tracks. The z information of the tracks is greatly improved by a procedure of fitting all tracks to a common vertex. The resulting precision of vertex determination in the z plane is around 1 cm [8].

The relatively poor z resolution of the CJC's is compensated for by the Central z chamber COZ and the Central Silicon Tracker CST [10]. The CST and COZ cover the polar angular range $16^0 < \theta < 156^0$. The z coordinate has an internal resolution of about $200\ \mu m$ for the COZ and of 12 μm for the CST. The vertex fitted tracks recognized in the CJC are supplied with information from the z chambers. As a result the vertex resolution is improved to 2 mm and the measurement of θ for individual tracks is improved from 20 to 2 mrad.

The Forward Track Detector FTD shown in fig.3.2 is designed to provide an accurate measurement of charged particle tracks and transversal momenta with the precision of $\sigma_{\theta,\phi} < 1mrad$ and $\sigma_{p_T}/{p_T}^2 < 0.003\ GeV^{-1}$. The forward tracker is consist of three drift chamber super modules. The angular coverage of the forward tracker is $7^0 < \theta < 25^0$.

A detailed simulation study shows that tracks reconstructed in the H1 Forward Tracker Detector FTD can be extrapolated back to the FST with a spatial resolution

of 2 mm and can be associated to FST tracks. The combined track momentum resolution translates to an r - ϕ impact parameter resolution for single tracks of about 90 μm which should be compared to the mean decay lengths of charm and beauty particles above 100 μm. This may allow a direct detection of charm decays.

3.2 The Silicon Trackers

As can be seen in fig.3.3 the H1 detector has three Silicon trackers: The Forward, Backward and Central Silicon Tracker, FST, BST and CST, respectively.

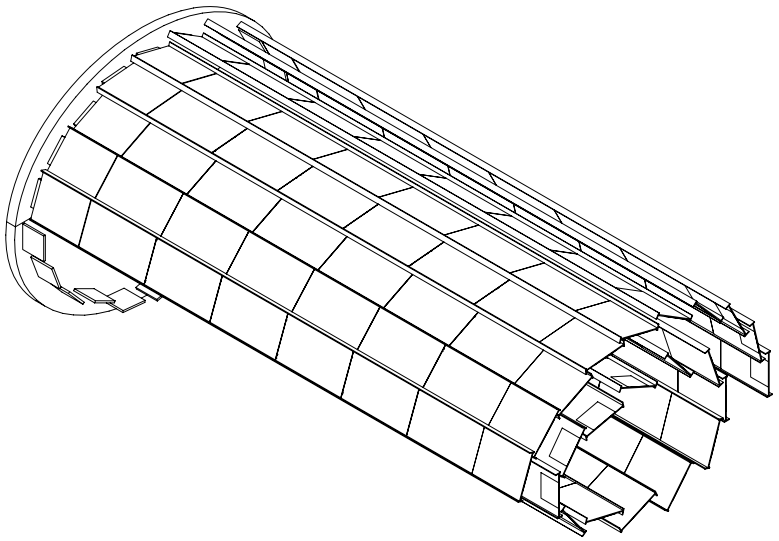

Figure 3.4: The H1 Central Silicon Tracker

3.2.1 The Central Silicon Tracker CST

The Central Silicon Detector CST shown in fig.3.4 consists of two concentric cylinders with radii at 5.75 cm and 9.7 cm, respectively, and a length in z direction of 35.5 cm. Its angular acceptance covers the whole azimuthal range and a polar range of $30^0 < \theta < 150^0$ for both layers. The efficiency of linking CJC tracks to CST hits in both layers is 85% [11]. A deep inelastic scattered event in the CST is shown in fig 3.5.

The coordinates are read out separately for ϕ (called p-side) and z (called n-side) and combined afterwards. Wrong combination of ϕ and z side coordinates (ghosts) and noise add significantly to the hit multiplicity. Suppression of noise has been tuned by rejecting hits with different signal-to-noise ratio on the p-side and on the n-side [12].

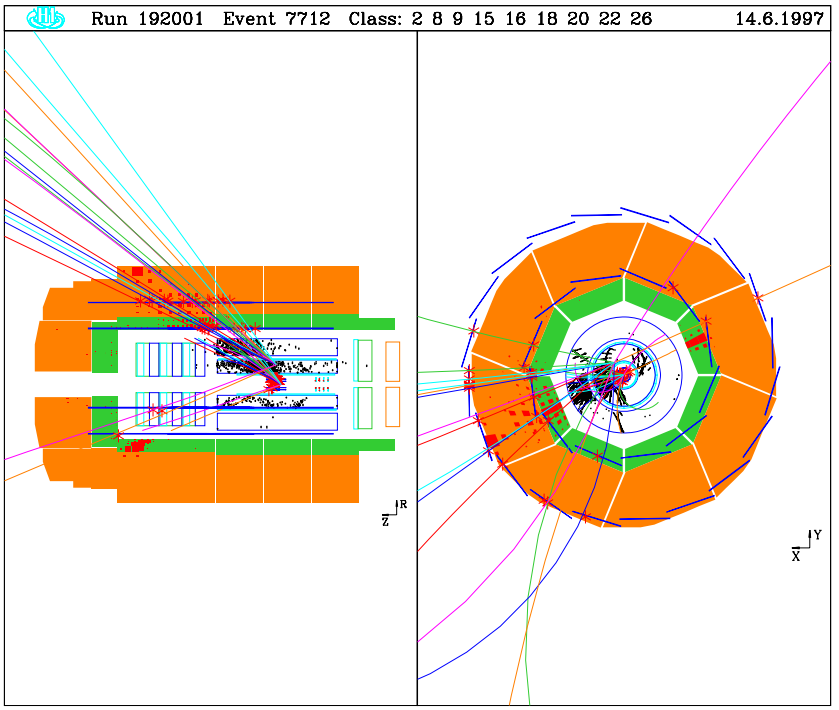

Figure 3.5: DIS event in the CST. In the x-y view the CST is strongly enlarged and superimposed to the H1 Central Tracker and Liquid Argon Calorimeter.

3.2.2 The Forward Silicon Tracker FST

The Forward Silicon Tracker FST is designed to measure forward scattered electrons [1] in the region of very large Q^2 which implies high x through $Q^2 = s \cdot x \cdot y$. This is the region where electroweak processes start to contribute to the cross section. Its polar angle coverage of $6^0 < \theta < 18^0$ roughly covers the θ range of the H1 Forward Tracker as can be seen in fig.3.6. The identification of the scattered electron or positron is profiting from the precise reconstruction of the lepton track segments in the FST in front of the dead material of the central and forward drift chamber systems. This extends the cluster track link and improves the vertex reconstruction efficiency for very forward angles [13].

The Forward Silicon Tracker is described in detail in the next chapter.

3.2.3 The Backward Silicon Tracker BST

The Backward Silicon Tracker BST was installed in 1996 and gradually upgraded each year. Its structure is very similar to the FST described in chapter 3. An overview of the BST and FST mechanics is presented in fig.3.7. The BST consists of 6 z planes equipped with detector modules. Each module consists of a sensor containing the silicon structure and a hybrid with readout electronics. There

[1] Due to the definition of the H1 coordinate system this corresponds to backward scattering in the spirit of Rutherford.

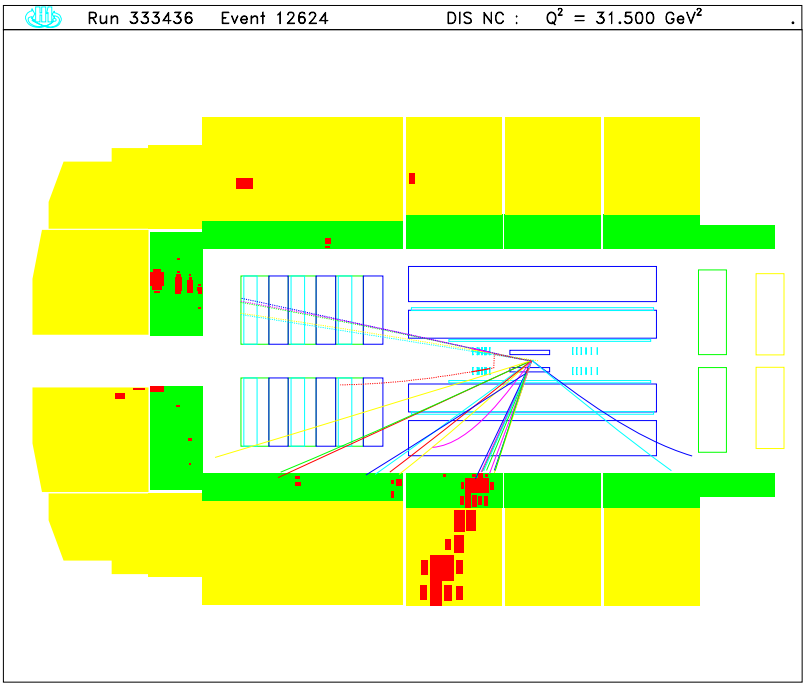

Figure 3.6: A high Q^2 neutral current event in the H1 detector. The scattered positron is measured in the FST and later totally absorbed in the electromagnetic calorimeter.

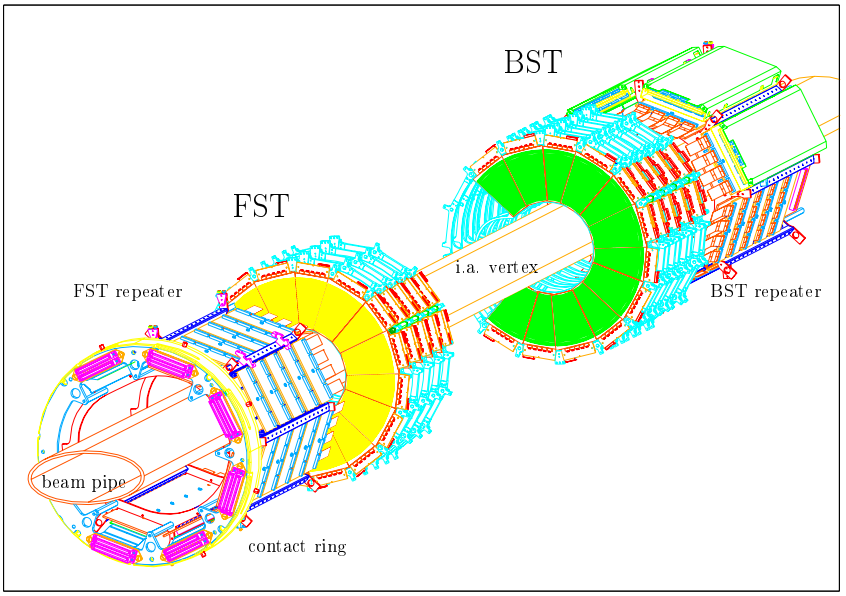

Figure 3.7: The BST and FST mechanics with the planes of Silicon sensors, the carbon fiber mechanical support structures and the repeater electronics.

are three types of sensors: u and v detectors, and the pad detectors. They serve to trigger on backward going charged particles.

The u and v sensors are shown in chapter 3. They are mounted back to back to form a z plane. Each BST plane has 12 azimuthal sectors. Four sectors are left empty to house the elliptical beam pipe. The overall length of this detector is 103 cm. The active volume occupies only 27 cm. The θ angular coverage is between 163^0 and 174^0.

The BST measures the scattered electron at low Q^2 and hadrons at low x in the backward region. The resolutions are $19\mu m$ for the r sensors and $12\ \mu m$ for u and v sensors. That has a big influence on the reconstruction of kinematics variables.

Chapter 4

The Forward Silicon Tracker

Chapter 5

Forward Silicon Tracker - FST

5.1 Silicon as Detector Material

Silicon is a semiconductor. It can be fabricated in two forms: n type, with a surplus of electrons in the crystal lattice, and p type, with a deficit of electrons in the crystal lattice .

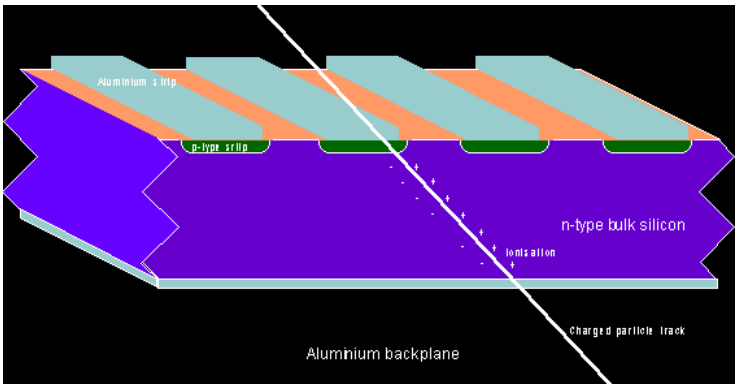

Figure 5.1: Illustration of a particle which deposits ionization while passing the silicon strips.

The majority of silicon detectors consists of n type bulk material. The back face has an aluminum contact over the complete surface. The front face has p type silicon strips implanted in the surface. These p type strips have aluminum strips in their surface. Those strips are separated from their associated p type silicon strips by a thin insulator. An electric field is applied between p strips and the back face .

When a charged particle pass through a silicon detector it creates ionization in the bulk of the silicon as is shown in fig.4.1. This frees electrons from the silicium atoms and leaves them with an electron vacancy. These vacancies are referred to as holes. The holes drift in the electrical field towards the negatively charged p type strips. The electron drift towards the positively charged back plane. When the holes reach the p type strip they are collected and induce a measurable charge on the associated aluminum strip. They are connected to sensitive read out channels. By

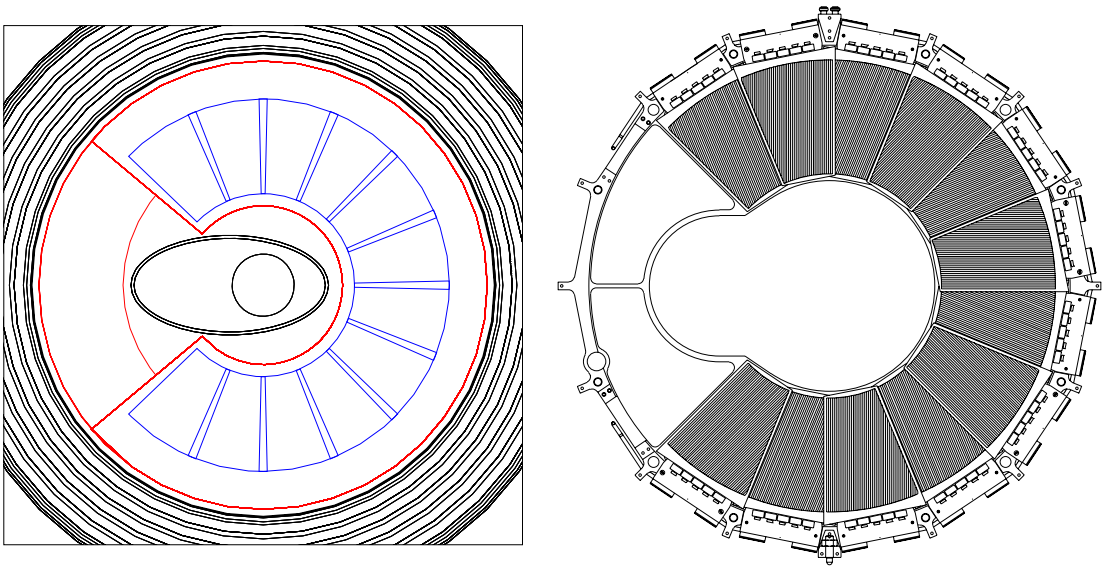

Figure 5.2: GEANT simulation and CAD pictures with the FST detectors arranged azimuthally around the beam pipe.

recording which electrical channel fired is possible to determine where the charged particle passed through detector.

5.2 Mechanics and Electronics

The structure of the FST is determined by the available space between the elliptic beam pipe and the mounting tube which is attached to the Central Inner Proportional Chamber CIP. In fig.4.2 we see that the shape of the FST is limited due to the elliptical beam pipe to 12 out of 16 possible azimuthal sectors. For positron running of HERA the $x-y$ interaction point is nearly at the center of the H1 coordinate system while for electrons the interaction point will be close to the center of the elliptical beam pipe and hence, strongly exentric to the FST.

The FST consists of 5 u and v planes mounted back to back and 2 later added r planes. The planes are arranged in z between 35 and 50 cm as shown in figures .4.3 and 4.5. The positions are not equidistant, but follow a harmonical series.

The silicon sensors are trapezoidal as shown in fig.4.2. They are mounted at 12 of the 16 ϕ positions per plane. The u-strips face the vertex, and the v-strips face the readout electronics. Strips of the u-detector cross the strips of the v detector under an angle of $180^0/16 = 22.5^0$ in the $x-y$ plane.

The FST has a total mechanical length in z of 75 cm with an active length of about 15 cm [fig.4.5]. It covers the θ angular region from 6^0 to 18^0 . The r detectors are added to increase the tracking redundancy. The u and v strip information is combined to reconstruct $x-y$ hits that allow circle track fits in the $x-y$ plane.

The FST voltage distribution and line driver electronics is placed on repeater boards close to the detector [fig.4.5]. Contrary to the BST all cables have to en-

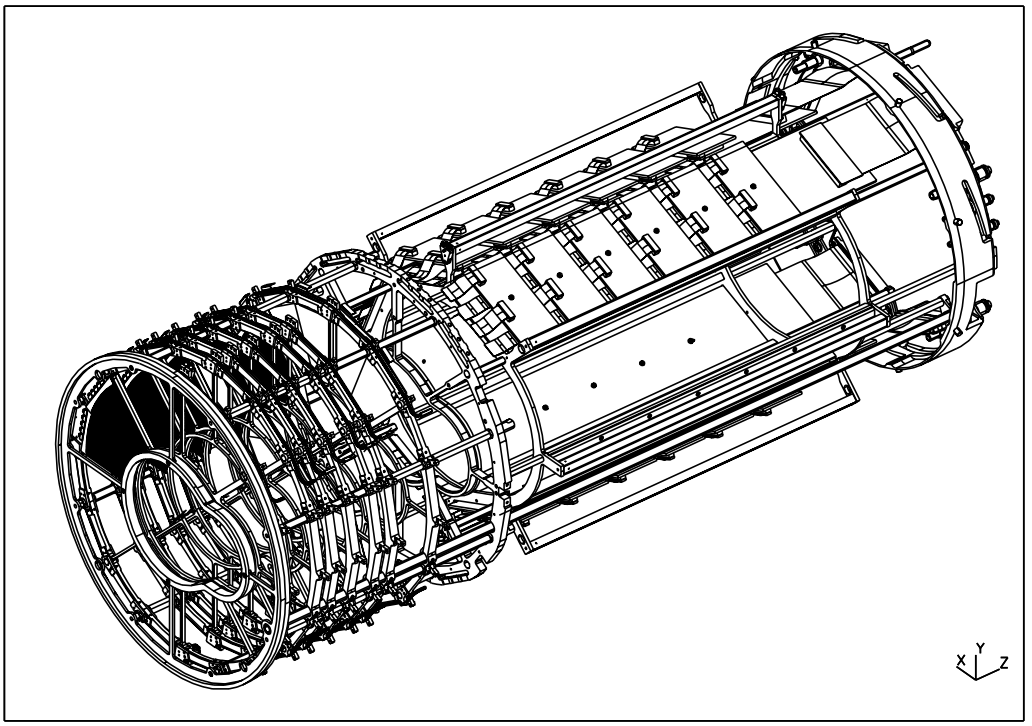

Figure 5.3: The FST mechanics with the carbon fibre skeleton (left) and the repeather board (right).

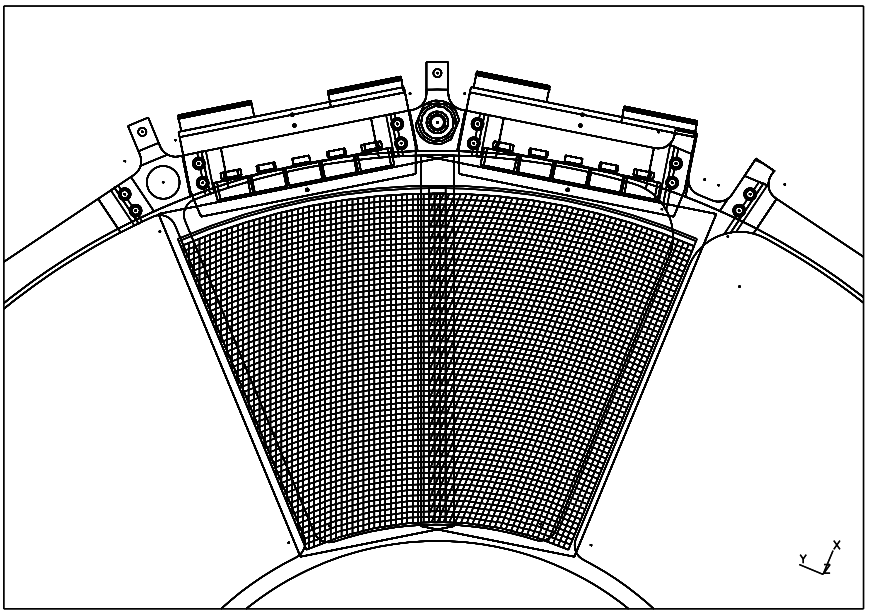

Figure 5.4: A pair pf u and r silicon sensors superimposed with the hybrid containing five APC's card.

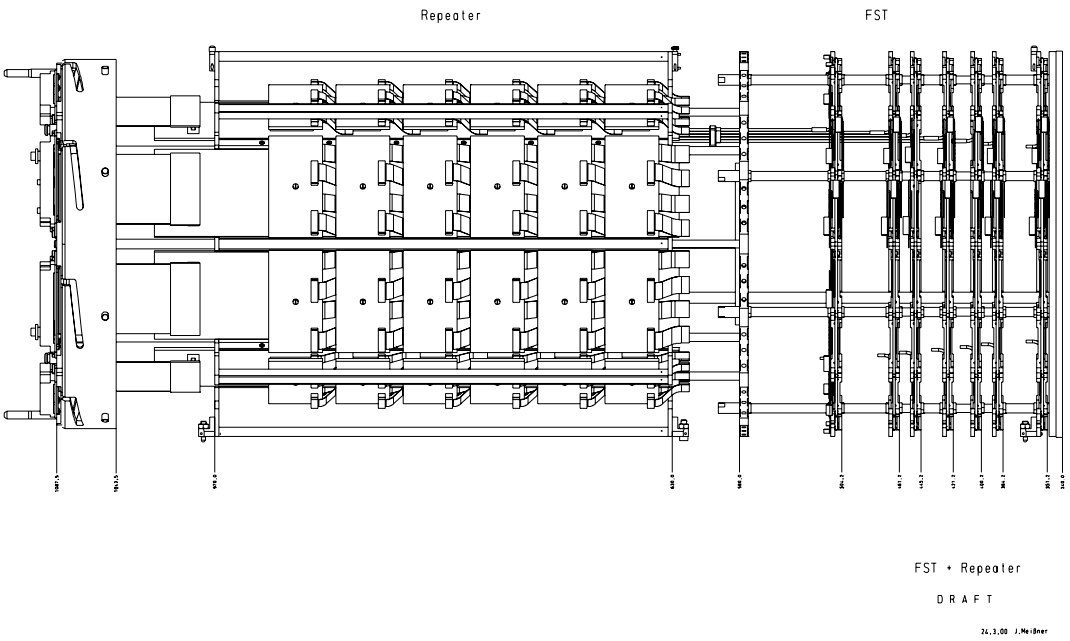

Figure 5.5: Side view of the FST repeater with the five u and v and the two r planes.

ter from the forward direction, through the gap between the Forward and Central Tracker. There is a special installation procedure where a cable and pipe fixing ring is placed at the end of the Central Tracker. This ring is connected to the 24 signal and control cables of the FST. The contact ring is fixed inside the silicon detectors mounting tube.

The FST dissipates a power of about 50W in the detector volume while each repeater board adds another 10W to the heat load. A water circuit provides cooling at the contact ring which has thermal contact to the repeater. The FST is split into an upper and a lower half, as the BST, in order to allow its installation around the beam pipe.

The FST includes 102.400 electronic channels with fully assembled planes. The detectors are read out by the Analogue Pipeline Chip (APC) [14]. It contains a storage array of 128 channels, each 32 events deap, with one trigger time slice being read out serially. Five APC's are placed on the hybrid to read out the 640 channels of one silicon disk.

This chip requires 14 control signals which are derived from a dedicated decoder chip. The Decoder is controlled by four clock signals which are generated in the sequencer part of the OnSiRoC module [15]. The analogue output signals of two hybrids (1280 channels on the line) are buffered on the repeater and fed through cable via an adapter card to the PowerPC based RIO modules.

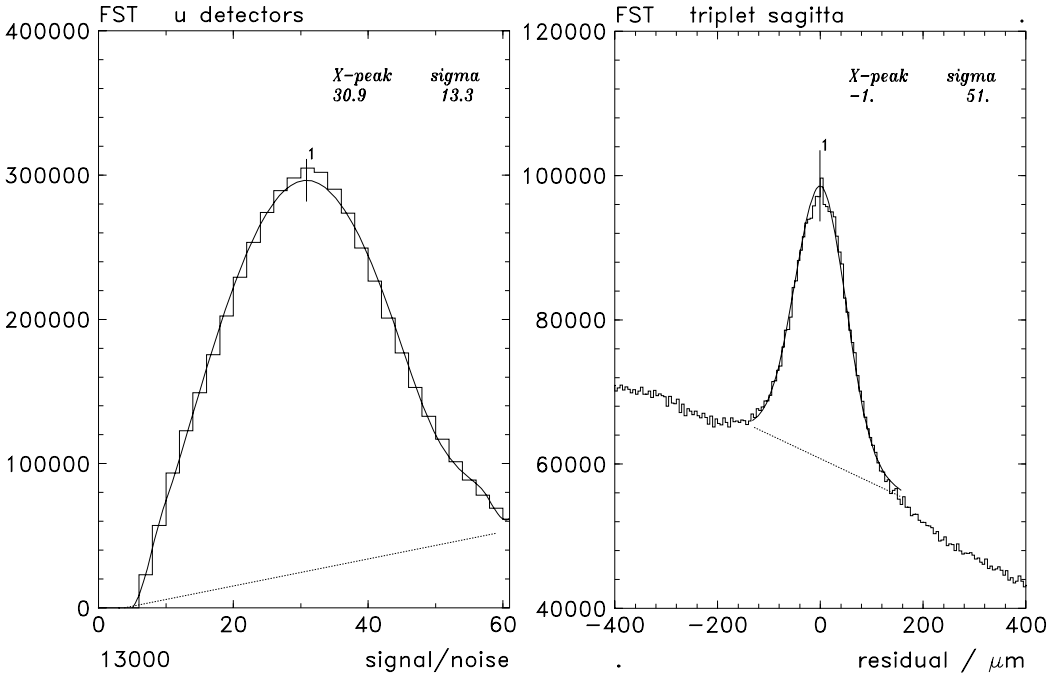

Figure 5.6: The signal-to-noise ratio and the raw combinatorial sagitta for the u FST detectors.

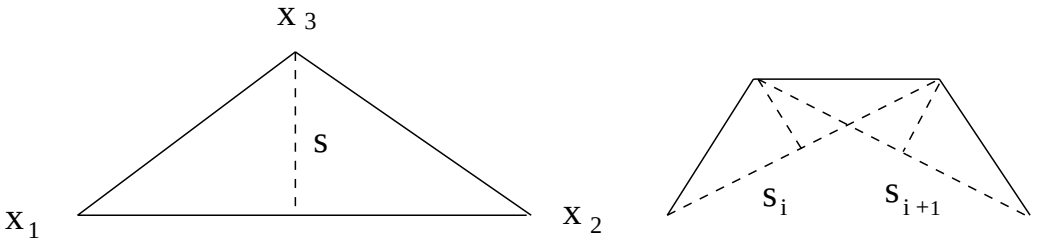

Figure 5.7: The triplet sagitta: S = $(x_1 + x_3)/2 - x_2$

5.3 The Track Reconstruction

The FST reconstruction consists of four steps:

1. **Hit finding and fitting:** The raw data from SIFE banks (FST + CST + BST raw hit banks) are clustered to hits packed in the BRSE and BRUE banks (r and u digitization banks respectively) for the BST r and u detectors and in the FRSE bank for the FST detectors.

The signal-to-noise ratio for the u detectors is about 30 as shown in fig 4.6.

2. **Pattern recognition:** Pattern recognition starts from the triplet sagitta. The sagitta S = $(x_1 + x_3)/2 - x_2$ is calculated for three subsequent hits as shown in fig.4.7. The sagitta is zero for a straight line and constant for circular tracks. The sagitta is easy to calculate. If the number of measurements is small it can work

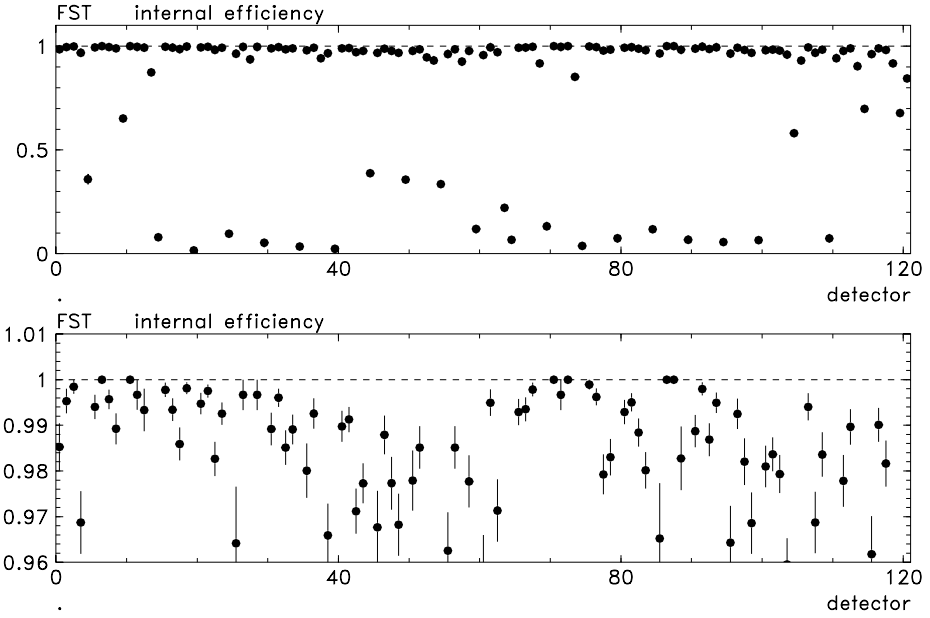

Figure 5.8: The FST efficiencies. They are close to 1 except for detectors in the last z plane.

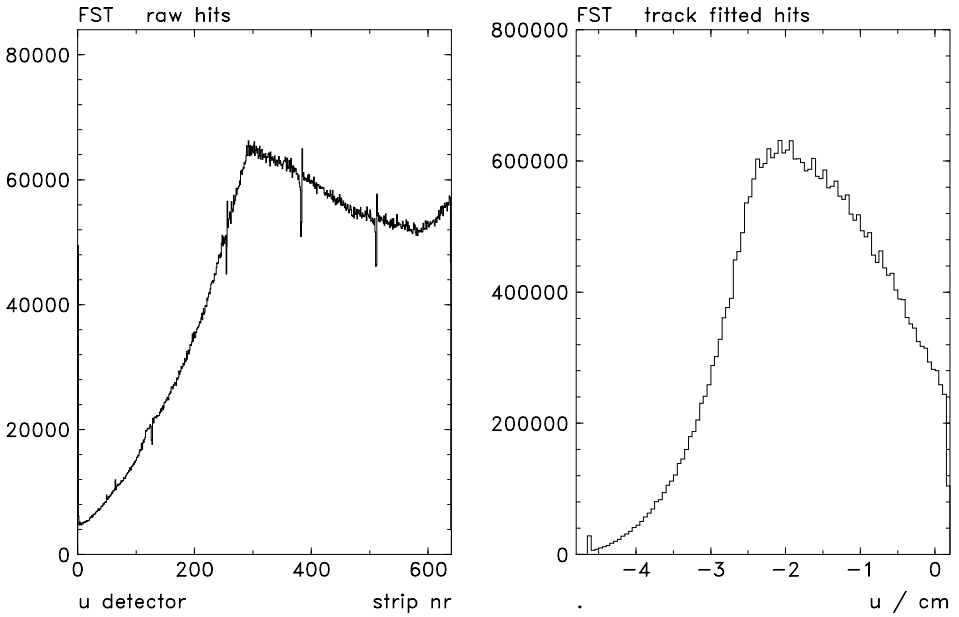

Figure 5.9: The FST occupancies: left: the number of raw hits per strip and right: the density of track fitted hits in u.

combinatorially .

the pattern recognition rejects noise and background and creates track candidates. The width of the raw combinatorial sagitta distributions as shown in fig.4.6.

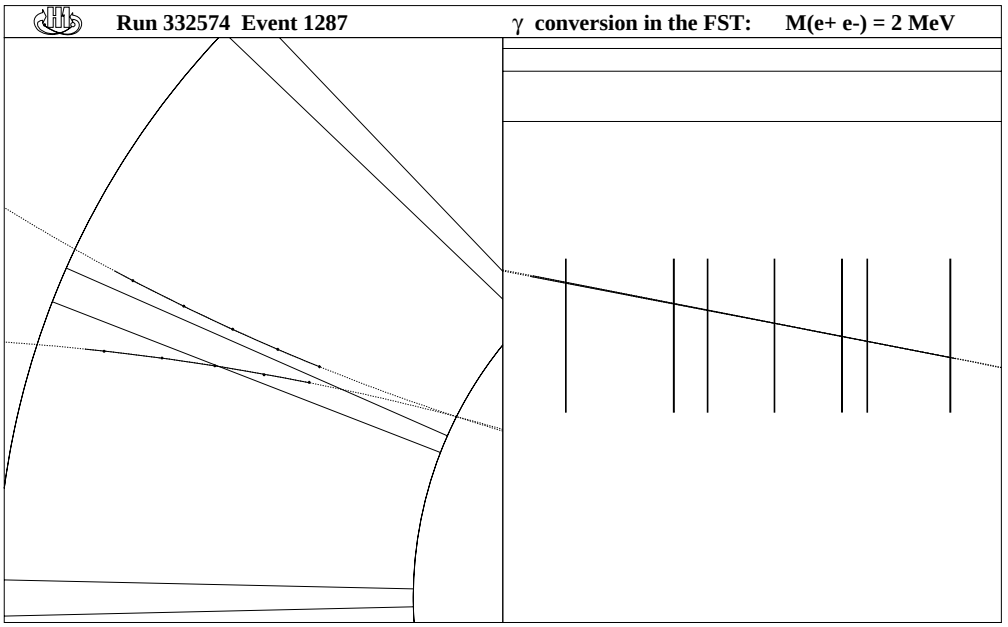

Figure 5.10: A photon conversion in the FST with an invariant mass of 2 MeV in the $x-y$ view (left) and $r-z$ view (right). Both electron tracks pass all five FST planes. As can be seen from the $r-z$ view the photon opening angle is zero due to the zero photon mass.

3. **3D track reconstruction and helix fit:** The track reconstruction consists of track finding and track fitting as illustrated in fig.4.10. For reconstruction of tracks we use the fact that a charged particle in a homogeneous magnetic field moves along a helix.

Track reconstruction starts when $u-z$ and $v-z$ 2D track candidates are combined to 3D $x-y-z$ points. Now, the mapping function apply the global alignment transformations to the 3D space hits which can be written out and visualized in the H1 event display.

Then circles are fitted in $x-y$ which gives three track parameters: the curvature, the azimuthal angle ϕ and distance of closest approach d_{ca}. Using the results of the circle fit straight lines are fitted in $s-z$ (s is the arc length) giving the polar angle θ and the z intercept z_0. The event vertex can be included to both fits. The default is to include the $x-y$ run vertex vertex to the $x-y$ circle fit but to avoid this in the $s-z$ fit.

The resulting five parameters of the helix are stored in the FJKT track bank in the H1 coordinate system. Transformations to vertex coordinates are left to the user.

4. **Monitoring:**

During online reconstruction the following quantities are monitored:

- Hit related detector properties like the signal-to noise ratio, raw and fitted occupancies [fig.4.8] and efficiencies [fig.4.9]

- Track related alignment and reconstruction properties like sagitta [fig.4.6], residuals and vertex pointing.

Chapter 6

Simulation and Reconstruction of K^0 Decays and Photon Conversions

6.1 Description of the Monte Carlo Code

Monte Carlo programs are tools to simulate the behavior of a given detector. In detail they are used:

- to generate event and particle kinematics,
- to track a particles through the detector,
- to simulate the detector response with a certain precision and
- to estimate the systematic uncertainties associated with the measurement.

As discussed in the motivation the luminosity in 2002-2003 was of the order of a picobarn hence, no serious physics could be done. So we decided not to use a specific Monte Carlo code generating a particular physics cross section. We rather preferred a simple and fast inline Monte Carlo generator where we generated the kinematics of a single test particle with a uniform distribution in the three space variables momentum and azimuthal and polar angle.

Then we simulate the detector behavior. For this purpose we defined all subdetectors, their positions (angles and positions with respect to the H1 coordinate system) and the material from which there are made. From this follows the geometrical acceptance of the detector. For example the FST can only accept tracks inside the angular range of $6^0 < \varphi < 18^0$ limited by the layout of the detector.

Now we simulate the response of the detector. This includes: smearing the response to the assumed detector resolution of 12 μm, as well as imposing noise and detector inefficiencies.

All particles interact in the dead material of a detector (beam pipe, mechanics, cooling, electronics) as well as in the active detector material (silicon, gas). Hence, every particle suffers a lot of physics processes: multiple scattering, energy loss, bremstrahlung, photon conversions, δ electrons, nuclear interactions, etc. All this effects are simulated in detail in the GEANT Monte Carlo program.

6.1.1 Track Parametrisation

In the homogeneous magnetic field track of charged particles are characterized by five helix parameters, three in the $x-y$ plane orthogonal to the magnetic field and two in the $r-z$ plane parallel to the magnetic field:

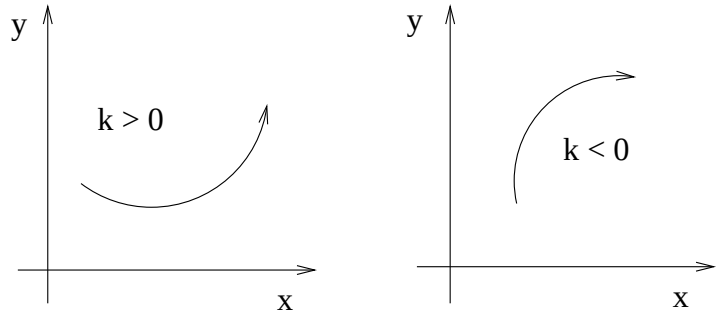

Figure 6.1: Definition of the curvature k = 1 / r

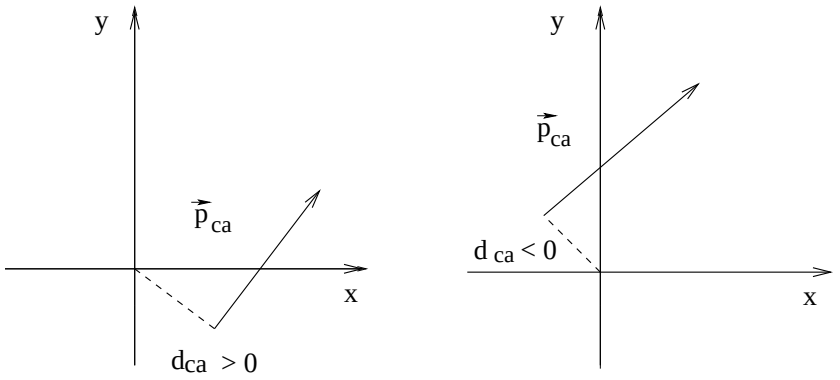

Figure 6.2: Definition of the distance of the closest approach d_{ca}

- the signed curvature $k = \pm 1/r$ which is the inverse track radius r. It is positive if the track propagates counter-clockwise as shown in fig.5.1.
- The signed closest distance d_{ca} from the origin of the (x, y) plane, shown in fig.5.2. It is positive if the vector to the point of closest approach and the trajectory direction form a right-handed system.
- the azimuthal and polar angles ϕ and θ as shown in fig.5.3 and
- the z-position z_0 at the point of closest approach is described in chapter 5.

The first three parameters are determined by a circle fit to the data in the $x-y$ projection using the non-iterative linearized algorithm of Karimaeki [16]. The circle equation is expressed in polar coordinates (r, ϕ) as:

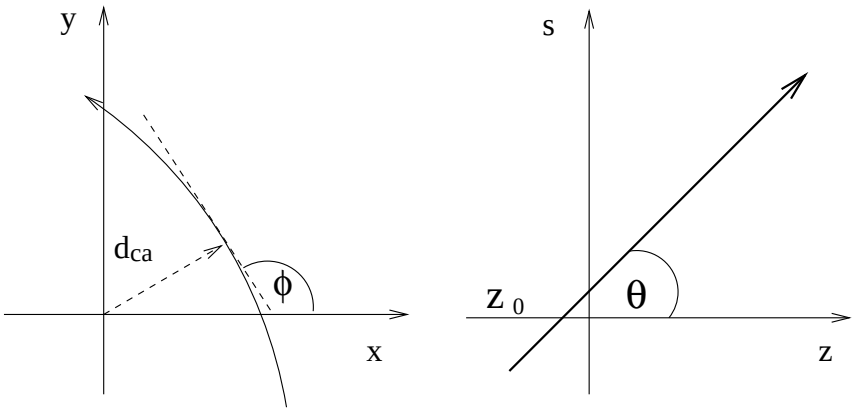

Figure 6.3: The azimuthal angle ϕ and the polar angle θ

$$\frac{1}{2}k(r^2 + d_{ca}^2) + (1 - k \cdot d_{ca}) \cdot r \cdot sin(\phi - \varphi) - d_{ca} = 0 \tag{6.1}$$

The other two parameters are determined by a linear least-squares fit of $z_i = z_0 + S_i \cdot tan\ \theta$, where S_i is the track length for the point z_i in the $x - y$ projection, with $S = 0$ at the d_{ca}. The slope parameter dz/dS is determined by the polar angle through $tan\ \theta = dS/dz$.

6.2 Reconstruction of K^0 Decays and Photon Conversions

The CJC V^0 finder code was used in order to reconstruct K^0 meson and photon conversions (in further text named as V^0s). However, due to the different geometry and precision , it had to be strongly adapted to the FST. Two processors were used: one for K^0 mesons and another for photons which we employ separately and also together. In the last case priority was given to the reconstruction of the K^0 mesons.

Neutral kaons were identified through the decay $K_S^0 \rightarrow \pi^+\pi^-$ channel and photons through the conversion $\gamma \rightarrow e^+e^-$ in the beam pipe and the dead material of the CST and FST in front of the FST sensors. For the K_S^0 analysis all $\pi - \mu - e$ and $K_S^0 \rightarrow 2\pi^0 \rightarrow 4\gamma$ decays we rejected in the Monte Carlo.

The H1 magnetic field is inside the Central Tracker CT homogeneous enough that we can describe, in the $x - y$ plane the orbit of a charged particle as a circle. The radius R is given as:

$$R = \frac{p_T}{c \cdot B} \tag{6.2}$$

with p_T the transverse momentum.

The reconstruction of the V^0s starts by asking for pairs of oppositely charged tracks. Next we determine crossing points. There we have a couple of cases:

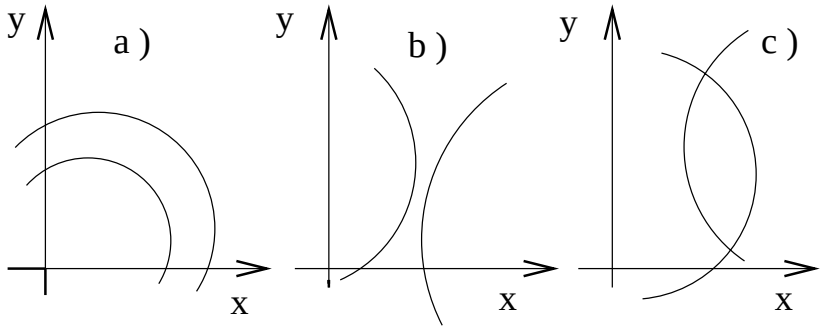

Figure 6.4: Possible cross point for two tracks : a.) two circles containing each other and b) circles excluding each other, c) circles with two crossing points.

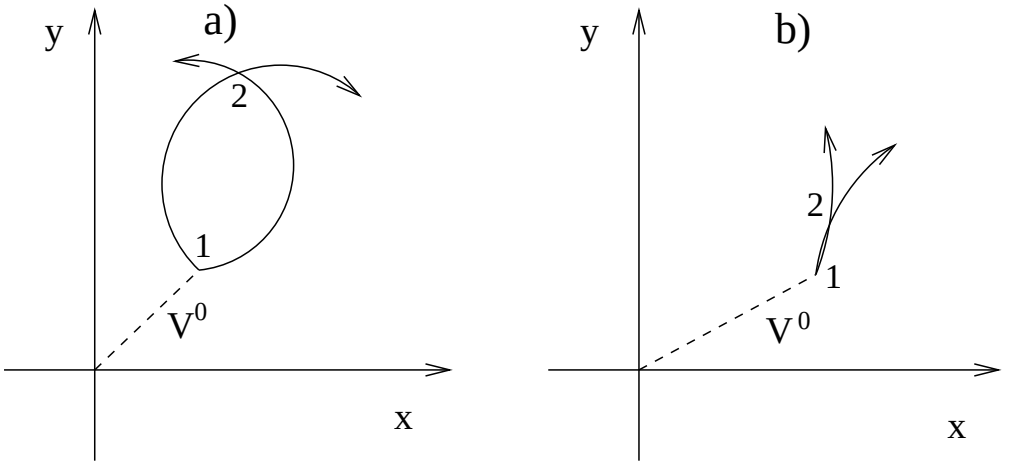

Figure 6.5: Types of V^0 decays: a.) The "cowboy" type. One interaction point can be safely rejected, b.) The "photon" type : Assuming zero opening angle, the two interaction points are accepted and the average value is taken.

1. Tracks which are not touching each other. For not touching tracks there are two cases as shown in fig.5.4: a) the case of circle in a circle and b) the case of separated circles. There we consider how far tracks are from each other. We reject cases where the sum of the x and y components of the d_{ca} is larger then 2 mm since they are to far to be considered as coming from the same vertex.

2. Tracks that have two crossing points, fig.5.4 c).

Photon conversions and K^0 decays have to be treated fundamentally different as shown in fig 5.5. Since photons have zero mass their decay opening angle is zero. Due to the finite values of tracking errors this automatically leads to two intersection points. On the other hand, K^0s at low enough momenta have large opening angles. This leads to a clear separation of the two solutions into a probable and an improbable one, so that only the better solution is taken instead of averaging two solutions as done in the photon case.

Candidates for neutral particles decaying into two charged particles are further tested by performing a constrained fit to the secondary vertex under the constraint of p_T conservation. In addition for photons a zero opening angle is imposed.

The FST bank structure was chosen in close analogy to the CJC banks. The FST reconstruction FSTREC produces FJKR banks containing the track five vector. After a vertex fit, the number of track parameters is reduced to the three vector (1/r, θ, ϕ) which is proportional to the particle momentum. At the same time, a mother vertex FSKV is created which absorbs the position information of the track: the z and d_{ca} of a track go into z and x, y of the mother vertex.

6.3 Characteristics of V^0 Reconstruction

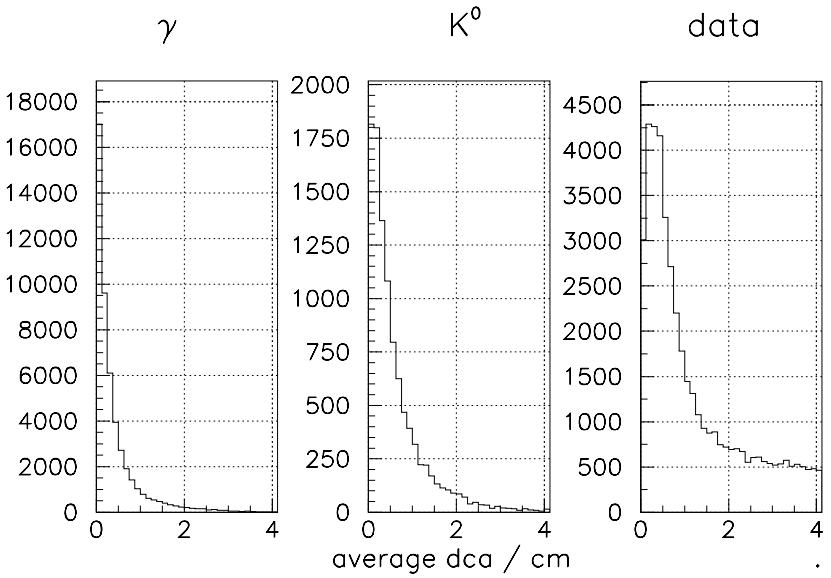

Figure 6.6: The average value of the distance of the closest approach of the two V^0 decay tracks.

We used the following characteristic quantities in the case of the V^0 reconstruction: the average distance of closest aproach d_{ca} of the two tracks, the length of the pointing radius, the errors of the polar and azimuthal angle σ_θ and σ_φ. To reduce combinatorial background and to ensure a good determination of crossing points i.e. secondary vertex cuts were imposed to all these quantities.

The distributions of the mentioned variables for photon conversion, K^0 decays and data are shown in fig.5.6 and fig.5.7. For the average d_{ca} we chose a cut at 1 cm for both photon and K^0, to ensure a good tangibility and to reject bad solutions of the reconstructed decay tracks. For data the distribution of the same value is wider because of background and noise which are removed by this cut.

The second parameter is the pointing radius [fig.5.7]. As shown in fig.5.8 it is defined as the length of the tangent from the origin to the track circle. For K^0

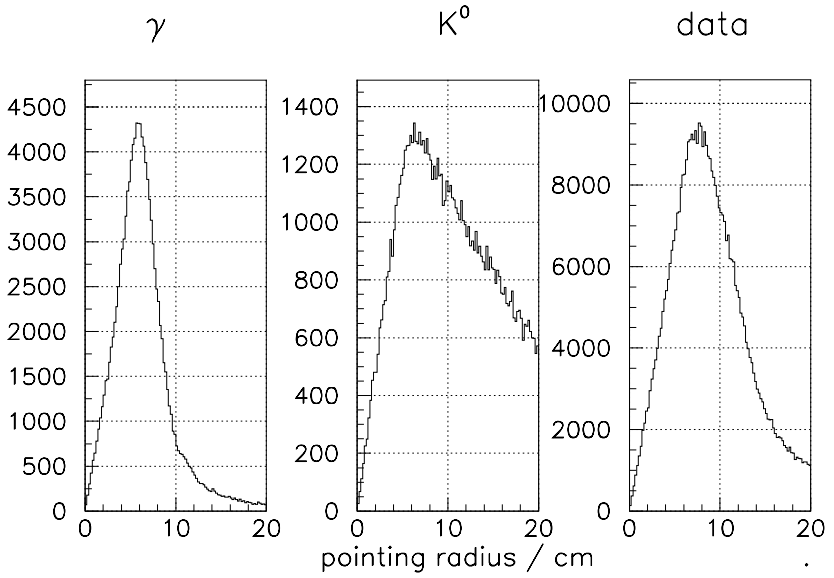

Figure 6.7: The distribution of the radius pointing to the decay vertex.

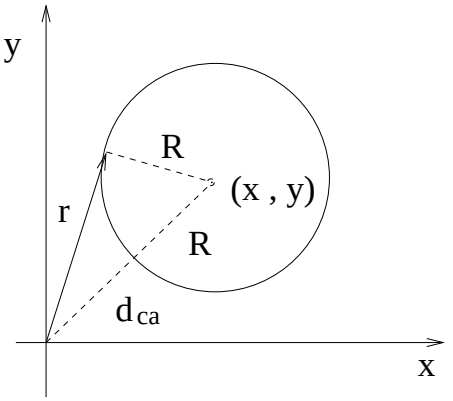

Figure 6.8: The definition of the pointing radius

decays it is larger due to the bigger opening angle then in photon case. To reduce the number of bad tracks we demand for tracks with a radius above 1 cm. The data distribution is simular to the photon Monte Carlo distribution which is mostly defined by the positions of the conversion material.

The behavior of the polar angle error σ_θ is visible in fig.5.9. There exist two peaks. The first one is for the case when all 5 planes are hit and the other one when 4 planes are hit. For photon and K^0 we have almost the same behavior which is reasonable in Monte Carlo. There we require that tracks have $\sigma_\theta < 2^0$. In data there are more 4 hit tracks since during some periods of data taking some of the planes could not be read out.

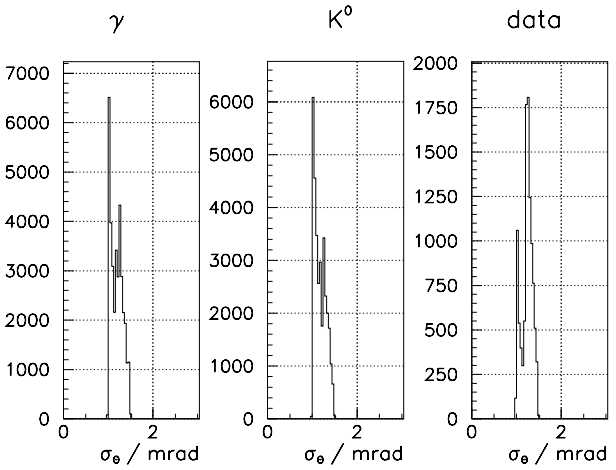

Figure 6.9: The distribution of the error of the polar angle σ_θ

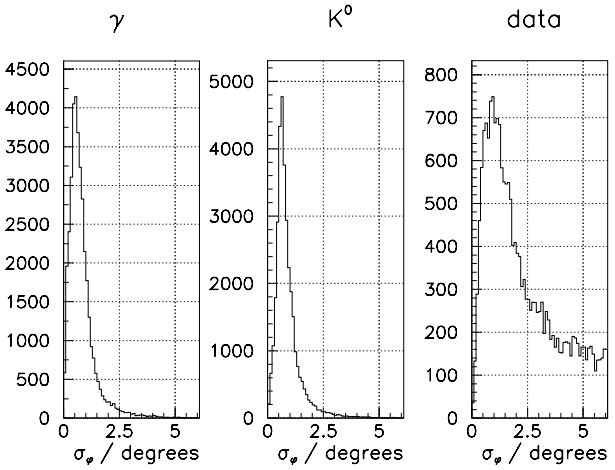

Figure 6.10: The distribution of the error of the polar angle σ_φ

The distribution of the azimuthal error σ_φ is shown in fig.5.10. All tracks that have $\sigma_\varphi > 3^0$ where rejected. In data we remove a lot of background by the above cut.

Bad tracks ware also reject applying more cuts:

- tracks with less then 4 hits were rejected,
- tracks with a χ^2 probability $p\,(\chi^2) < 0.001$ were rejected,
- tracks in the silicon overlap regions were rejected to avoid artificial combinatorics.

Chapter 7

Monte Carlo Analysis

7.1 Photon Conversions

7.1.1 The Precision of the Photon Conversion Vertex

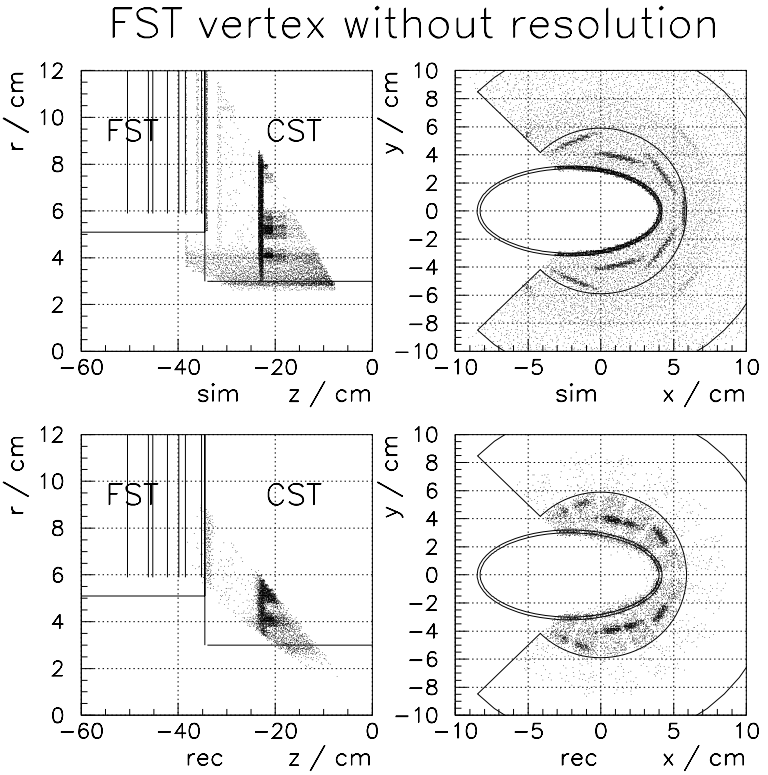

Figure 7.1: The r-z and x-y view of the simulated and reconstructed photon conversion vertex without FST resolution .

To present a better understanding of the simulation and to ensure a good reconstruction we first considered the photon conversion vertex. In fig.6.1 are shown the

simulated and reconstructed conversion point of the photon without FST resolution. The beam pipe is clearly visible in the x-y plane. The structure of the CST mechan-

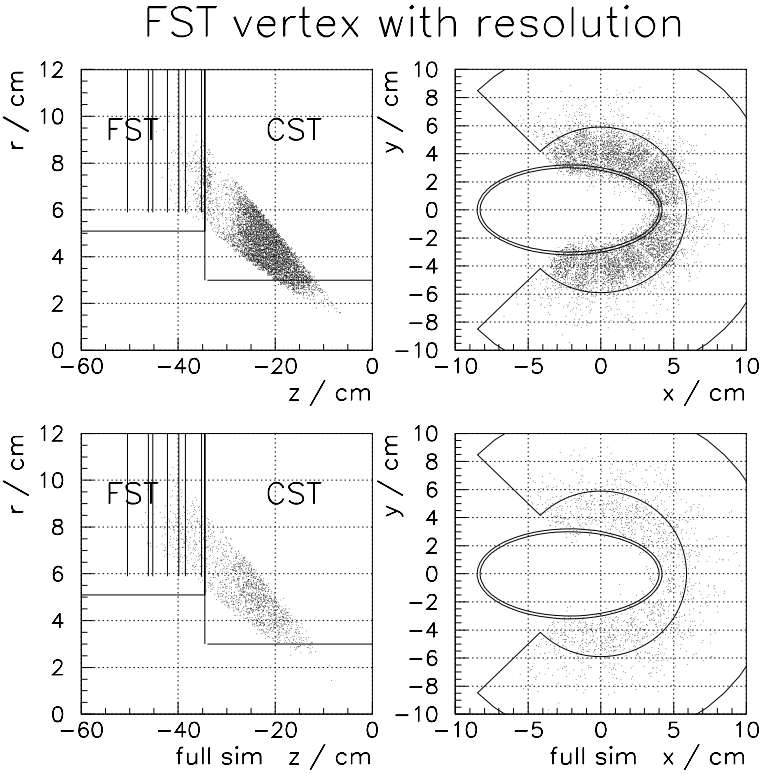

Figure 7.2: The r-z and x-y view of the reconstructed photon conversion vertex with 12 μm FST resolution and with all physics processes included.

ics, cooling and electronics are also visible where additional conversions arise. In the r-z plane the positions of the FST and the CST and of beam pipe are emphasized. We took only conversions which happened up to the second FST plane since we are asking in the reconstruction for at least 3 hits in the track finding and 4 hits in the track fitting routine. So since we have to fit the vertex we need one additional degree of freedom hence, we need 4 hits.

For the reconstructed photon conversions the geometrical acceptance of the FST is visible which is between $6^0 < \theta < 18^0$. The vertex is smeared into the interior of the beam pipe. Due to the rejection of the tracks in the overlaps the boundaries between the silicon sensors are visible.

Figure.6.2 shows the reconstructed photon conversion vertex with the FST resolution of 12 μm and by inclusion of all physical processes. Evidently the statistics is lower due to failures in fitting caused by the frequent electromagnetic interactions which sometimes reach the straingth of showers.

7.1.2 Photon Reconstruction Errors

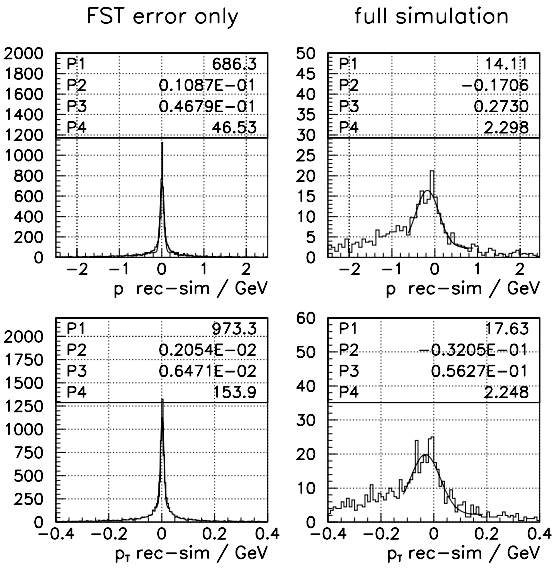

Figure 7.3: The resolutions of total and transverse momentum p and p_T with the FST resolution of 12 μm and including physics processes, calculated from the differences of the simulated and reconstructed values.

In order to measure the resolution of the photon momentum reconstruction we observe the differences between reconstruction and simulation of: the momentum p, the transverse momentum $p_T = p \cdot tan\ \theta$, the polar and azimuthal angles θ and φ, as well as the r and z coordinate of the conversion vertex in the H1 coordinate system.

In fig.6.3 are shown the distributions of the momentum errors for the case where we consider the FST resolution only and for the case when we also simulate all physical processes. From our resolution of 12 μm for u and v detectors we get a fairly good reconstruction of all variables. The second histogram shows however, a much wider distribution due to the inclusion of the physical processes (electromagnetic interactions of the e^+e^- pairs). The distribution of p_T is narrower by factor of $tan\ \theta \approx 0.2$ as for p which is reasonable.

As we can see on fig.6.4 the resolutions for θ and φ are around 1 and 6 mrad, respectively. Also these values are dominated by the physical processes.

Fig.6.5 shows the differences between reconstructed and simulated values of of the conversion point in r and z. The r resolution is about 8 mm if we consider the FST full simulation which includes physical process. Again we see a factor of five between the z and r resolution. From fig.6.6 one can see that is difficult to precisely determine the vertex due to the small photon opening angle. The vertex scatter plots in fig.6.1 and 6.2 also illustrate this problem.

For z that is even more obvious: fig.6.5 gives a z error of 1.7 cm relying on the FST resolution only and about 4 cm if we consider physical processes also. By

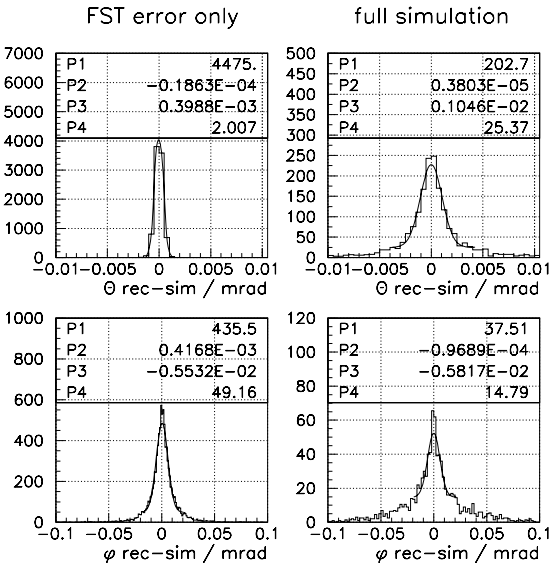

Figure 7.4: The resolutions of angular and azimuthal angles θ and φ with the FST resolution of 12 μm and including physics processes, calculated from the differences of the simulated and reconstructed values.

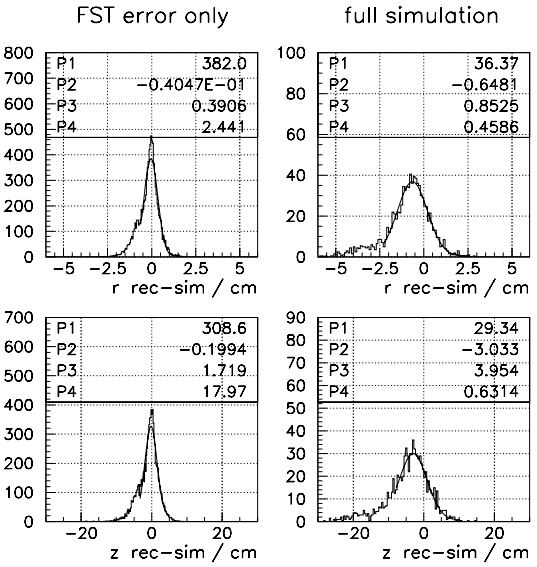

Figure 7.5: The resolutions of r and z positions of the vertex with the FST resolution of 12 μm and including physics processes, calculated from the differences of the simulated and reconstructed values.

comparison we can see a factor of five between the z and r resolution because of $cot\ \theta \approx 5$. For the $r - z$ view we can see also in fig.6.6 that events suffer from

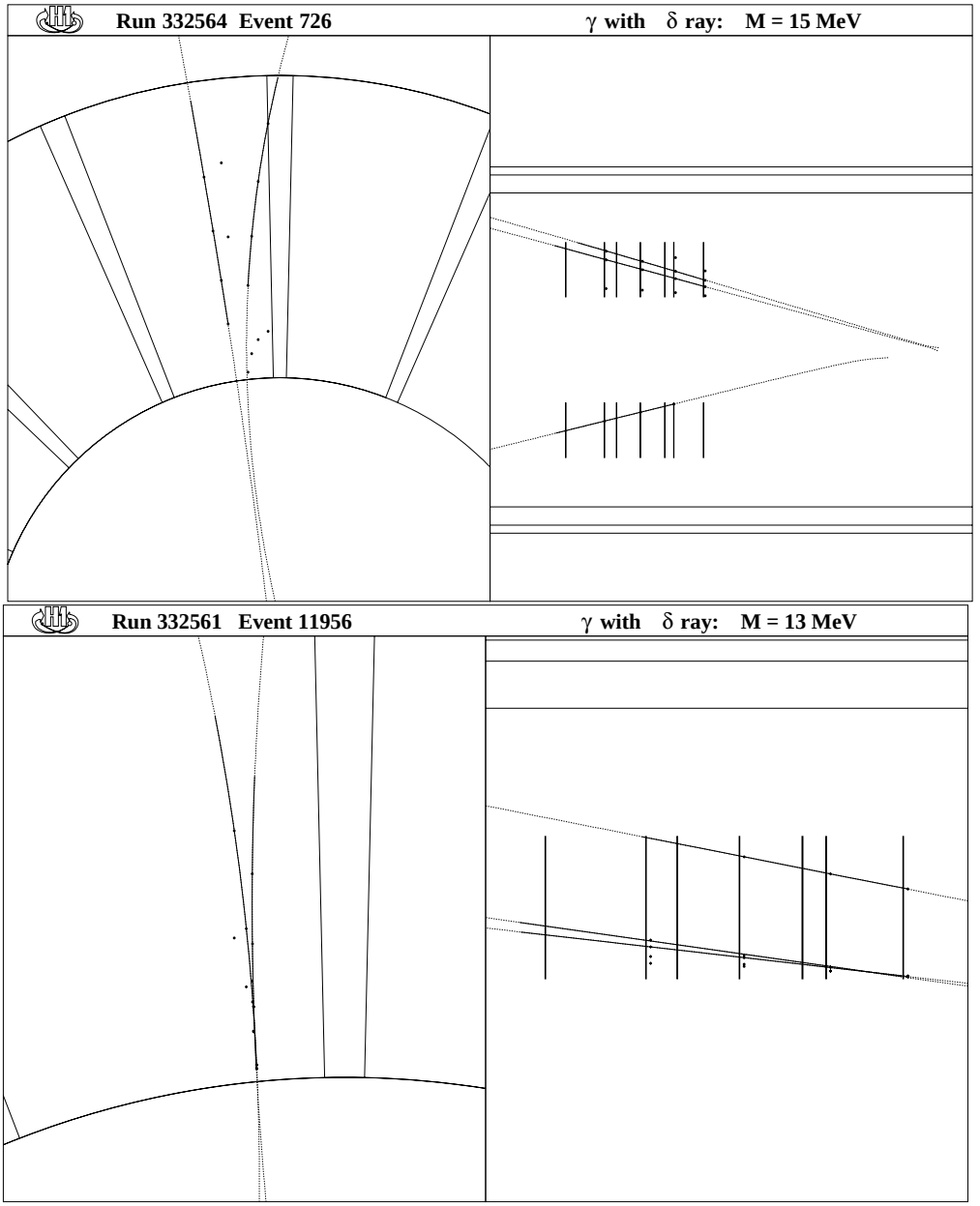

Figure 7.6: Photon conversions in the FST suffering from electromagnetic interactions: both events contain a delta ray. The opening angle is not anymore zero.

electromagnetic interactions. The polar opening angles which should be zero are smeared. Also, in $x - y$ plane the tracks do not anymore precisely touch each other. This deteriorates the mass resolution: both photon masses are above 10 MeV. In the $x - y$ view we also recognize the two mathematical solutions discussed in section 4.2: in event 726 the decay tracks miss each other due to the bad momentum resolution caused by the electromagnetic interaction. In event 11956 they cross each other delivering two solutions. This illustrates how all resolutions are deteriorated.

7.1.3 Photon Acceptance and Efficiency

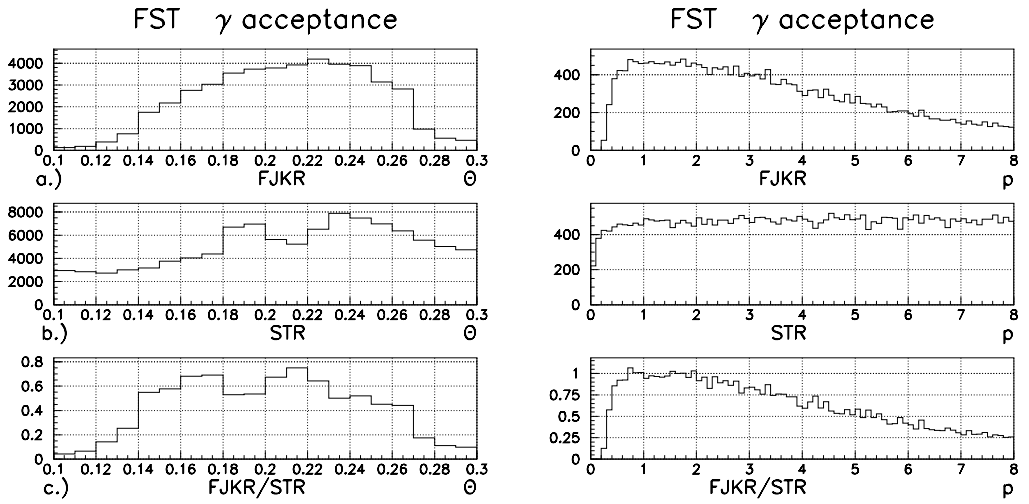

Figure 7.7: The distributions of: a.) the number of reconstructed events from FJKR banks, b.) the number of simulated events from the STR banks, c.) the ratio of the both giving the FST acceptance depending on θ and p.

The acceptance of events is mainly limited by the polar angle θ and momentum p dependence. In fig.6.7 is presented the number of events reconstructed by the FST reconstruction and the number of simulated events depending on θ and p. Division of those two histograms gives the FST acceptance for photon conversions. The distribution of simulated events in θ depends on the material allocation which is the reason of the non uniform distribution of events. The momentum averaged acceptance for photon conversions is about 60%.

For the momentum depending acceptance the simulated distribution is uniform. A small gap below 100 MeV is present because of momentum cuts in the GEANT and H1 simulations. Asymmetric photon decays enlarge this dip at low p for the reconstructed FJKR tracks. The FST photon acceptance between 0.5 and 2 GeV is close to 100 $\%$. This means that the FST track reconstruction is fully efficient in regions of the full acceptance. For low momentum the acceptance drops further due to a sagitta cut.

The number of V^0 fitted one events with two tracks divided by the number of reconstructed events gives the FST photon reconstruction efficiency [fig.6.8]. Its value reaches about 50%. Losses come from the demand for at least 3 hits in track reconstruction but at least 4 hits for the V^0 fit due to the absence of the primary vertex. This loss happens due to short track length and asymmetric decays. It also depends from where the conversion was. If the photon carries small momenta then it opens in θ and we can loose one of the tracks. These arguments become stronger at low momentum and induce the drop below p = 2 GeV.

After all mentioned demands and reasons the product of acceptance times effi-

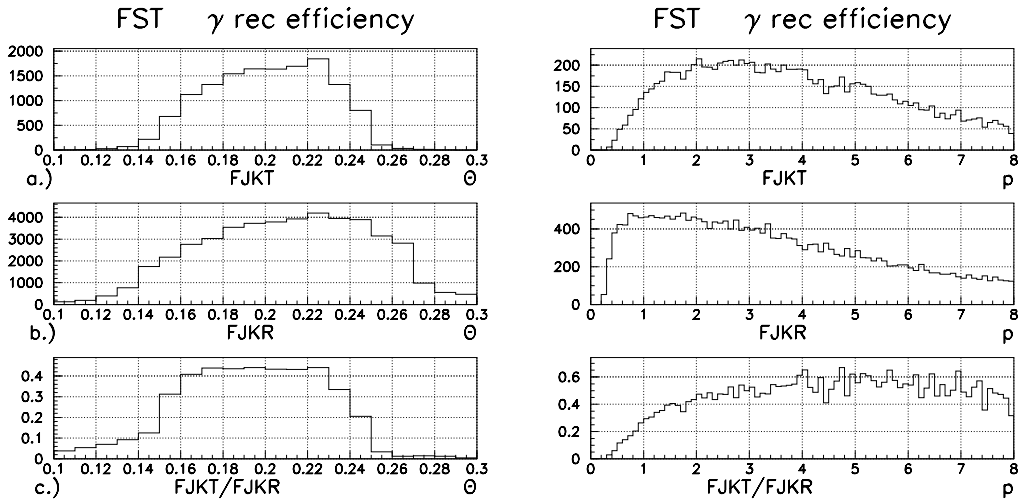

Figure 7.8: The distributions: a.) the number of V^0 fitted events from FJKT banks, b.) the number of reconstructed events from the FJKR banks, c.) the ratio of both giving the FST photon reconstruction efficiency depending on θ and p.

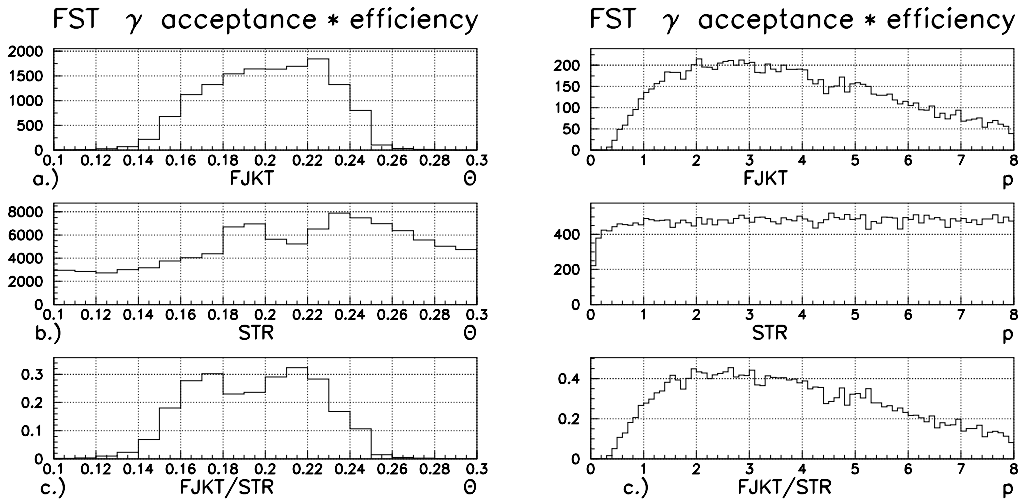

Figure 7.9: The distributions of: a.) the number of V^0 fitted events from FJKT banks, b.) the number of simulated events from the STR banks, c.) the ratio of both giving the FST acceptance times efficiency depending on θ and p.

ciency is shown in fig.6.9. It reaches 40% between 1.5 and 4 GeV.

7.2 K^0 Decays

7.2.1 K^0 Reconstruction Errors

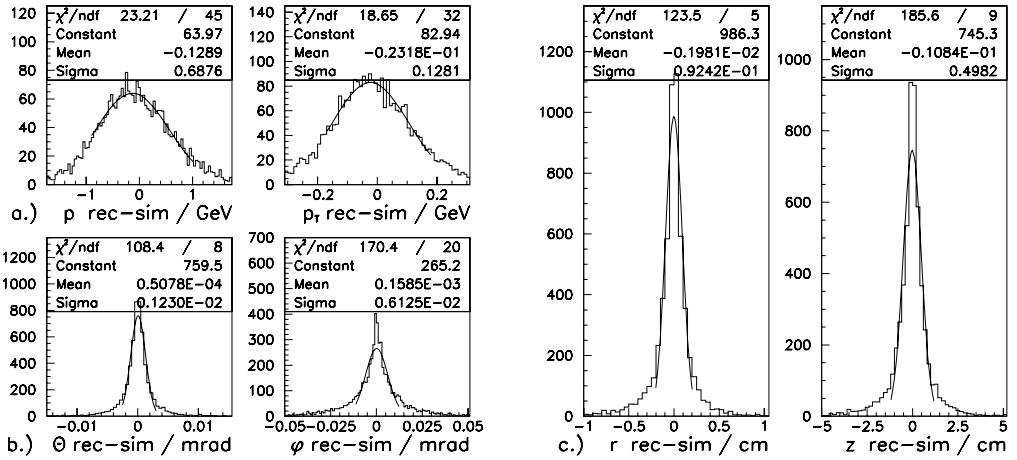

Figure 7.10: a.) The distributions of: the total and transverse momentum p and p_T, b.) the polar and azimuthal angles θ and φ and c.) of the decay vertex positions in r and z.

The same resolution study which was done for photon conversions was done for K^0 mesons also. In fig.6.10 are shown the differences of reconstructed and simulated variables for the total and transverse momentum p and p_T, polar and azimuthal angles θ and φ as well as the decay vertex positions r and z including an FST strip resolution of 12 μm and allowing all physical processes.

In these distributions we asked for: 0.475 GeV $< m_{K^0} <$ 0.51 GeV /c^2 and transverse momentum of daugther particles $p_T >$ 150 MeV /c .

It is visible from fig.6.10 that the resolutions for θ and φ are 1 and 6 mrad as for the photon. The resolution for the decay vertex positions r and z are about 1 and 5 mm respectively, again observing the geometrical relation between r and z.

In fig.6.11 the mass resolution of the K^0 mesons is shown with a width of 55 MeV. This is worse than in the central tracker for the following reasons:

- The CJC has about ten times more hits than the FST.
- In the FST only about one half of the decay length is covered by measuring points while in the Central Tracker nearly the full V^0 is measured. Since circle fits are non-linear this extrapolation error goes with the square of the extrapolated length.

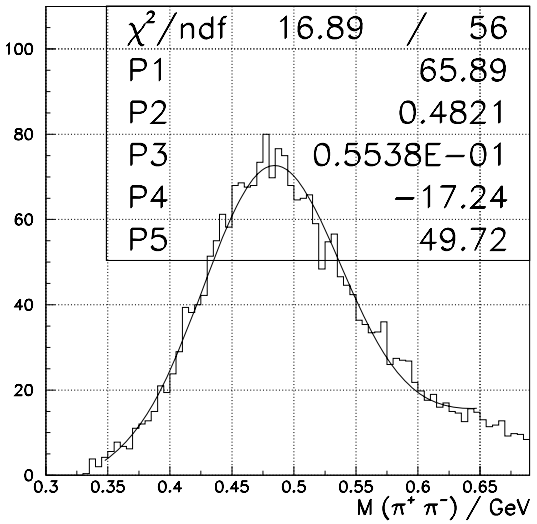

Figure 7.11: The reconstructed K^0 invariant mass distribution in Monte Carlo.

7.2.2 The FST K^0 Acceptance and Efficiency

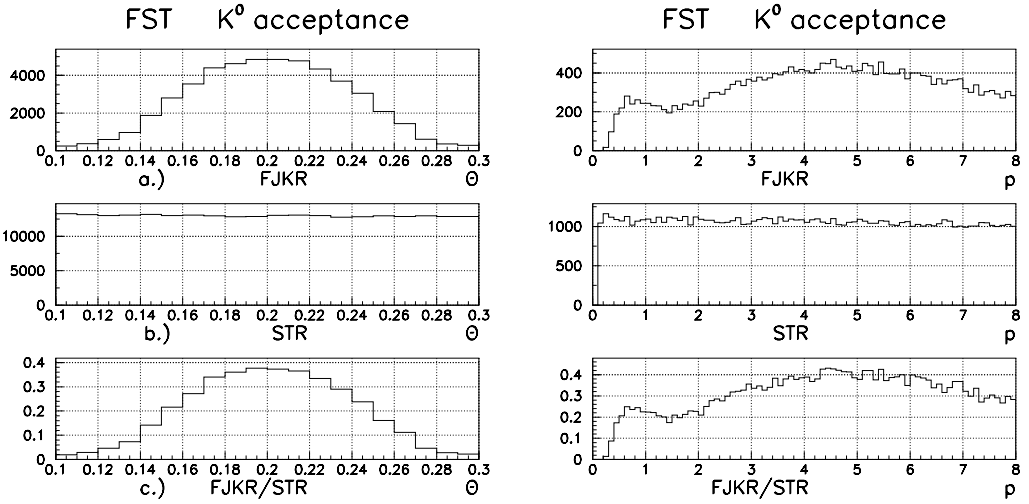

Figure 7.12: The distribution of: a.) the number of reconstructed K^0 events from FJKR banks , b.) the number of simulated K^0 events from STR banks, c.) the ratio of both giving the FST K^0 acceptance depending on θ and φ.

The acceptance of K^0 mesons is mainly limited by the scattering angle θ and momentum p dependence. In contrast to photon conversions neutral kaon decays have

a large opening angle due to the mass difference between mother and of daughter particles. The θ and p distributions are shown in fig.6.12. Looking on the θ dependence, the acceptance for K^0 mesons reaches 35%.

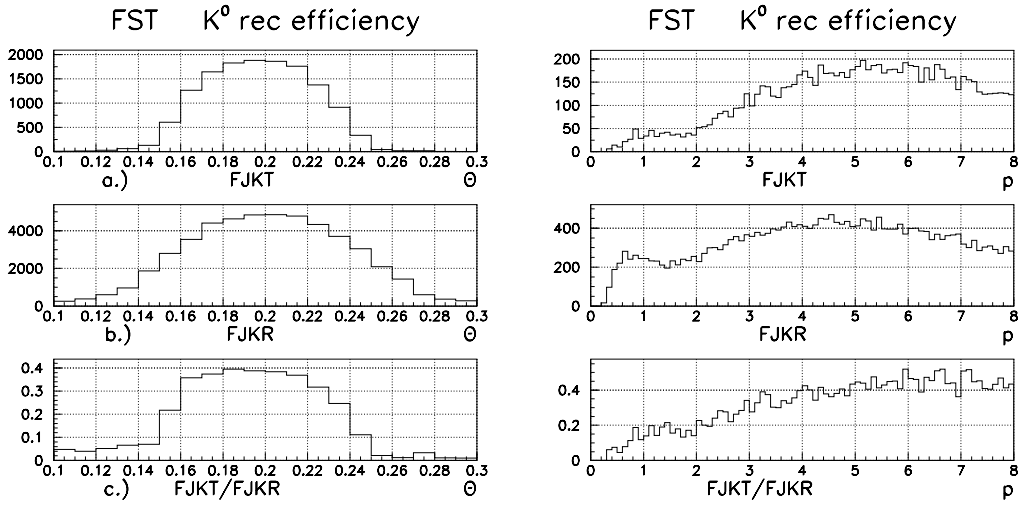

Figure 7.13: The distributions of: a.) the number of V^0 fitted K^0 events from FJKT banks , b.) the number of reconstructed K^0 events from FJKR banks, c.) the ratio of both giving the FST K^0 efficiency depending on θ and φ.

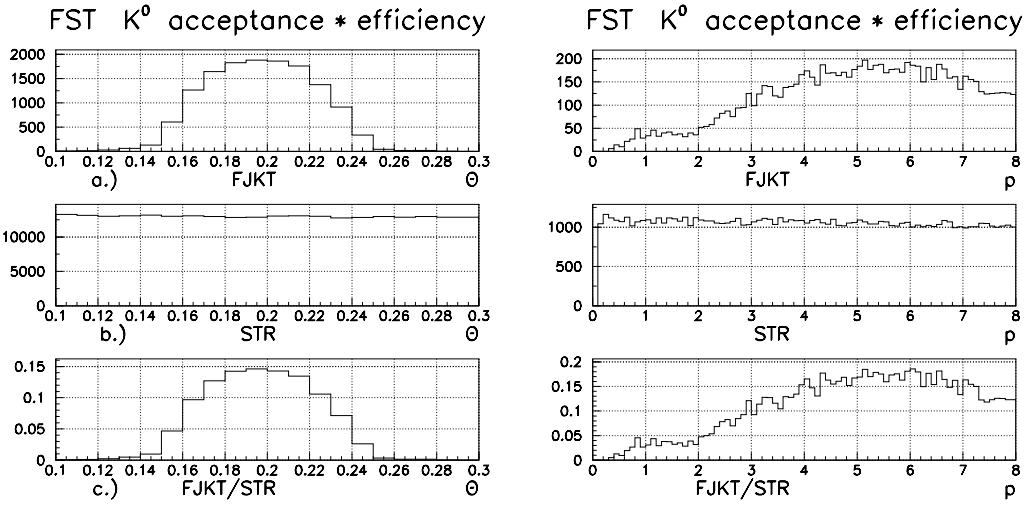

Figure 7.14: The distributions of : a.) the number of $V60$ fitted K^0 events from FJKT banks, b.)the number of simulated K^0 events from STR banks, c.) the ratio of the both giving the FST acceptance times efficiency depending on θ and p.

For simulated events a drop below $p = 100$ MeV is present in the p dependence

due to momentum cuts in GEANT and H1 simulation. At low momenta the acceptance is visibly lower due to decays close to the primary vertex which are enhanced at low momentum. For small decay lengths the K^0 decay particles have a small probability to reach the FST and to fulfill the demand of at last 3 hits in the reconstruction. On the other hand, at large momenta the K^0 tend to decay behind the FST.

The FST K^0 reconstruction efficiency reaches 40$\%$ in polar angle θ and p dependence as shown in fig.6.11. For small momenta the loss is greater because of the step from 3 hits in track reconstruction to 4 hits in the V^0 fit. Another reason for the low acceptance at low momenta is that for early decaying kaons we are forced to make long extrapolations to the decay vertex. Due to error propagation the probability to reconstruct is smaller.

The combined acceptance times efficiency is visible in fig.6.14. It reaches 15$\%$ at 4 GeV which is less than for photons. Below 2 GeV the acceptance falls under 5$\%$ due to above mentioned reasons. Finally, it drops to zero below 0.8 GeV.

As a summary, it can be said that for the K^0 the space resolution is good but the total efficiency is bad while for photon the efficiency is good but the space resolution is bad.

Chapter 8

The V^0 Algorithm in H1 Data

In 2002 and 2003 the FST received first data from HERA. The detector readout and the hit and track reconstruction were shown to work properly. Due to the HERA background conditions the useful luminosity in H1 was only of the order of an inverse picobarn so that no serious physics analysis could be performed. We used 350.000 preselected events covering data from June 2002 until to the run end in February 2003. The selected events contain at least one FST track.

8.1 The Photon Conversion Vertex

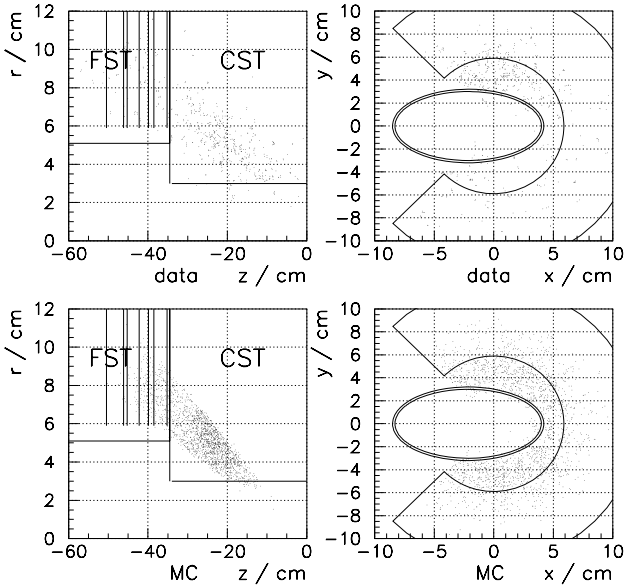

Figure 8.1: The r-z and x-y positions of the photon conversion point in H1 data and Monte Carlo.

We now compare the experimental data with Monte Carlo events. Major demands for the photon conversion are: transverse track momentum of $p_T > 25$ MeV /c and photon mass: $m_\gamma < 20$ MeV /c.

In order to generate four hits and to reject the conversions in the FST repeaters and end rings behind the FST, we ask the place of the conversion point to be in front of the second FST plane requiring $z < 38.5$ cm.

In fig.7.1 are shown the $r - z$ and $x - y$ positions of the photon conversion point for H1 data and Monte Carlo. First of all, as in Monte Carlo, we do not observe photon conversions inside the beam pipe. Next, we observe the same concentration of conversions in the region of the CST dead material as in Monte Carlo. This means that we are mostly observing photon conversions. As a third signature of a photon as a electromagnetic object we see accompanying delta rays both in data and Monte Carlo.

It is also visible that most of the data are concentrated in the upper half of the detector which may be due to distribution of the HERA background.

Due to the reasons mentioned in chapter 6.1.2 the r and z resolutions of the conversion vertices are not good enough to provide a detailed X-ray picture of CST, FST and the beam pipe.

8.2 The Photon Mass Distribution

In fig.7.2 we show the invariant masses of the photon in simulation and H1 data. The left plot assumes an FST error of 12 μm while for the central plot all physics processes were included. We simulated one million Monte Carlo events while the

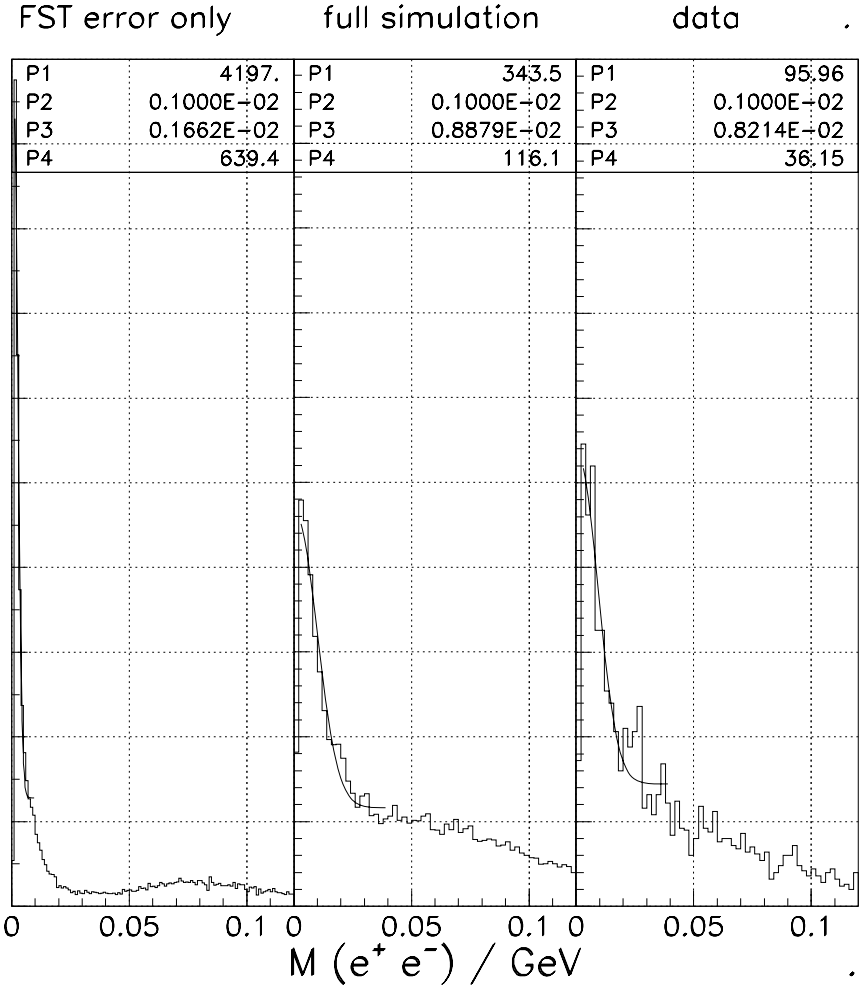

Figure 8.2: The invariant masses of the photon in simulation and H1 data. The left plot assumes an FST error of 12 μm. For the central plot all physics processes were included.

data statistic was around 350.000 FST selected events.

The Monte Carlo mass resolution of reconstructed photons including an FST resolution of 12 μm is only 1.6 MeV. If we include all physic processes it increases to 8.9 MeV while in data we get 8.2 MeV. This shows a good agreement between data and Monte Carlo analyses. It also shows that the whole reconstruction is dominated not by the FST precision but by electromagnetic processes in front of the FST.

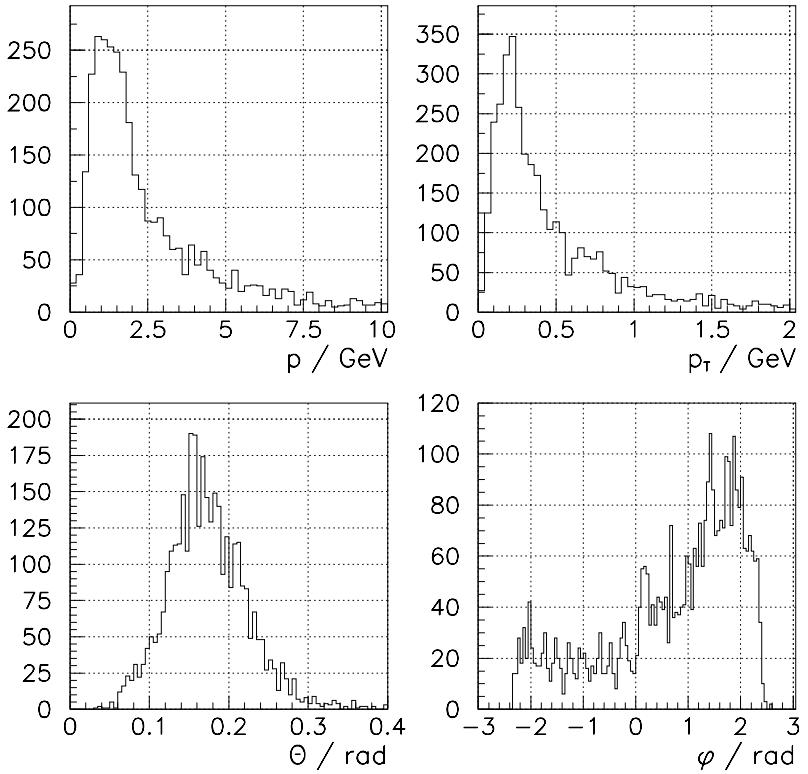

Figure 8.3: The distributions of the momentum p, transverse momentum p_T and the polar and azimuthal angles θ and φ.

8.3 The Distributions of Angles and Momentum

We now present in fig.7.3 spectra of the total and transverse momentum p and p_T and of the polar and azimuthal angles θ and φ of the photon recorded in the FST during the 2002/2003 running period. The momentum spectrum peak is at 1 GeV and the transverse momentum around 0.2 GeV. This is a reasonable value for jets with energies between 10 and 100 GeV going into the forward direction. The distribution of the polar angle θ reflects the geometrical acceptance of the FST which is $6^0 < \theta < 18^0$ or 0.10 rad $< \theta <$0.32 rad. The spread of the polar angle φ describes the acceptance in the $x - y$ plane which is limited by the elliptical shape of the beam pipe to $-135^0 < \varphi < 135^0$. Due to the harsh background conditions in the considered running period the φ distribution is not necessarily uniform as also observed in the H1 Background Report [20].

In conclusion, the above distributions have justified that our simulation and V^0 reconstruction algorithm were coded and used correctly.

8.4 Search for K^0 Mesons in FST Data

It was shown in fig.6.14 c) that below 2 GeV the combined acceptance times efficiency drops under 5% below 2 GeV and goes to zero below 0.8 GeV. This is

however, the region where the inclusive cross section is concentrated [**?**].

The FST acceptance is smaller than expected if we aim to measure more than a single particle. This is not only due to the small polar angle range of the FST. We also loose K^0 that decays in z behind the second FST plane as well as decays at low K^0 momentum close to the primary vertex since one of the tracks can miss the FST due to the large K^0 opening angle for low momentum.

In contrast to the photon case where we easily detected a prominent peak in the invariant mass spectrum no K^0 signal was observed in the invariant mass of the $(\pi^+\pi^-)$ system.

There are however, more reasons that make observation of K^0s more difficult:

- The production of strange quarks is suppressed by a factor of 0.2 with respect to the production of light quarks.
- The K^0 decays to 50% as ${K_S}^0$ and to 50% as ${K_L}^0$. The ${K_L}^0$ due to their long life time escape the FST.
- The ${K_S}^0$ has a 68.8% branching ratio into $\pi^+\pi^-$.

In conclusion, for the reasons given above the K^0 detection in the FST alone is an ambitious goal. Any future analysis of multi particle final states should include the whole H1 Central Tracker.

Chapter 9

Summary

The H1 Forward Silicon Tracker FST saw in 2002/2003 its first data from the upgraded HERA collider. Due to high background from HERA the useful luminosity of H1 was limited to about one inverse picobarn so that no serious physics analysis could be performed. However, the FST detector readout and the hit and track reconstruction worked properly.

In this Diploma thesis photon conversions and decays of neutral strange particles were used for a first test of the FST acceptance, performance and precision. To understand the experimental data and the software a simple and fast inline Monte Carlo generator and the GEANT package were used to generate the kinematics and basic physic processes of the test particles. In order to reconstruct K^0 decays and photon conversions a secondary vertex finder code was adapted to the completely different geometry and precision of the FST.

The results of this work are:

- The **acceptance** of the FST alone is primarily limited by the polar and azimuthal angles. Through the decay time it also depends on the momentum. The K^0 acceptance was measured as a function of momentum and polar angle and approaches 35% while the photon acceptance reaches 100%.
- We also determined the **efficiency** of the V^0 finder as a function of momentum and polar angle. It reaches 40% for K^0 and 50% for photons.
- In real data we identified **photons** through the distributions of their conversion points and delta electrons. The width of the experimental photon mass distribution of 8.9 MeV nicely compares with the Monte Carlo resolution of 8.2 MeV.
- We also studied the **resolutions** of momentum, polar and azimuthal angles and conversion and decay points. For photons, all resolutions are spoiled by the electromagnetic processes in the dead material. Nevertheless, the photon mass is precise enough to allow photon identification.
- For K^0s all above resolutions are better. However, acceptance and reconstruction efficiency are lower so that no K^0 mass peak could be observed.

We finally **conclude** that:

- The FST acceptance is smaller than expected if we aim to measure more then a single particle. This will be particularly important for the detection of charm final states or jets in the FST. Both should include the whole H1 Central Tracker.
- The material in front of the FST seriously influences the measurement of electromagnetic particles. This will be not only true for the photons studied here but also the scattered electrons at highest Q^2 which were one of the aims of the FST and the HERA luminosity upgrade.

Acknowledgments

It has been a great pleasure to have the opportunity to work in such a large experiment like H1. I want to thank to all people in Zeuthen and Hamburg that made this possible, specially to **Dr Peter Kostka** and **Dr Max Klein**.

Most of all I want to thank to **Dr Thomas Naumann** for his patience, supervision and very helpful advices during the past months. Thank you for introduction to the H1 Experiment, for all debugging, great ideas and for non selfish sharing of your knowledge.

Also, I want to thank to my professors **Doc.Dr Nataša Raičević** and **Prof.Dr Slobodan Backović** for their endless support, advices and for a million encouraging e-mails with the smiles and sun from the Montenegro.

Special thanks to **Doc.Dr Gordana Medin** who was with me from a first day of my staying in Germany and who became my great friend.

I would like to thank to all of my colleagues and new friends which gave me support and have a patience to deal with a lot of my questions and who had learned me that the German kitchen is not that bad. **Ewelina, Jan, Tomas, Mirek, Alexey, Ilya, Sergey** you made my staying here nicer, thank you for all fun in the spare time too.

I'm proud that I can thank to my friends at home who wrote me a detailed letters and keep encouraging me every day. I'm finally going to have a good time with them.

And last but not the least to my wonderful family: **my parents** who gave me a moral support and endless love, to my **twin-sister** which smile and presence I missed so much and to my **big brother** with his huge optimism and funny stories. I couldn't manage without you. You always kept me going.

Bibliography

[1] Thomas Naumann's web page: www-zeuthen.ifh.de/˜naumann/h1.

[2] G. Herrera, Univ. Dortmund, D Meson Production Asymmetries at the H1 (H1-Upgrade) Experiment, H1-IN-562(01/1999).

[3] P. J. Bussey, Heavy flavour physics at Hera- a survey, Gla-PPE/2001-04.

[4] R. Feynman, Phys.Rev.Lett. 23 (1969) 1415.

[5] I. Abt et al. (H1 Collaboration), Nucl.Instr.Meth. A386(1997)310.

[6] E. Elsen, The H1 Trigger and Data Aquisition System, H1 internal Note H1-01/93-262(1993).

[7] J. Burger et.al., NIM A279(1989)217.

[8] P. Thompson, Open Charm Production in Inclusive and Diffractive Deep-Inelastic Scattering at Hera, PhD(1999).

[9] Measurement of the $D^{*\pm}$ Meson Production and ${F_2}^c$ in Deep-Inelastic Scattering at HERA, H1 Collaboration, Phys.Lett.B, July 2001.

[10] S. Egli et al., NIM A 283(1989)487.

[11] D. Pitzl, The H1 Silicon Vertex Detector, et al. ETH Zurich , ETHZ-IPP PR-2000-1.

[12] S. Luders, CST/DP2000 Stand Alone Tracking and Vertexing, 1999.

[13] A Forward Silicon Tracker for H1, W. Braunschweig et al. H1-Note, H1-02/99-563.

[14] R. Horisberger and D.Pitzl, NIM A326(1993)92.

[15] J. Burger et. al., NIM A386(1997)269.

[16] V. Karimaeki, Fast code to fit circular arcs, Helsinki University report NU-SEFT-1991-10(1991).

[17] Particle Data Group, Phys. Rev.66(2002)1.

[18] Photoproduction of K^0 and γ at HERA and comparing with DIS, H1 Collaboration, May 1997.

[19] The European Physical Jurnal C, Particles and Fields, J. Bartels, D. Haidt, A. Zichichi, 1996.

[20] H1 note H1-01/03-607.